Am J Physiol Heart Circ Physiol 293: H2516–H2522, 2007.
First published July 20, 2007; doi:10.1152/ajpheart.00424.2007.

Angiotensin II attenuates myocardial interstitial acetylcholine release in response to vagal stimulation

Toru Kawada,[1] Toji Yamazaki,[2] Tsuyoshi Akiyama,[2] Meihua Li,[1,3] Can Zheng,[1,3] Toshiaki Shishido,[1] Hidezo Mori,[2] and Masaru Sugimachi[1]

[1]*Department of Cardiovascular Dynamics, Advanced Medical Engineering Center and* [2]*Department of Cardiac Physiology, National Cardiovascular Center Research Institute, Osaka; and* [3]*Japan Association for the Advancement of Medical Equipment, Tokyo, Japan*

Submitted 5 April 2007; accepted in final form 19 July 2007

Kawada T, Yamazaki T, Akiyama T, Li M, Zheng C, Shishido T, Mori H, Sugimachi M. Angiotensin II attenuates myocardial interstitial acetylcholine release in response to vagal stimulation. *Am J Physiol Heart Circ Physiol* 293: H2516–H2522, 2007. First published July 20, 2007; doi:10.1152/ajpheart.00424.2007.—Although ANG II exerts a variety of effects on the cardiovascular system, its effects on the peripheral parasympathetic neurotransmission have only been evaluated by changes in heart rate (an effect on the sinus node). To elucidate the effect of ANG II on the parasympathetic neurotransmission in the left ventricle, we measured myocardial interstitial ACh release in response to vagal stimulation (1 ms, 10 V, 20 Hz) using cardiac microdialysis in anesthetized cats. In a control group ($n = 6$), vagal stimulation increased the ACh level from 0.85 ± 0.03 to 10.7 ± 1.0 (SE) nM. Intravenous administration of ANG II at 10 $\mu g \cdot kg^{-1} \cdot h^{-1}$ suppressed the stimulation-induced ACh release to 7.5 ± 0.6 nM ($P < 0.01$). In a group with pretreatment of intravenous ANG II receptor subtype 1 (AT_1 receptor) blocker losartan (10 mg/kg, $n = 6$), ANG II was unable to inhibit the stimulation-induced ACh release (8.6 ± 1.5 vs. 8.4 ± 1.7 nM). In contrast, in a group with local administration of losartan (10 mM, $n = 6$) through the dialysis probe, ANG II inhibited the stimulation-induced ACh release (8.0 ± 0.8 vs. 5.8 ± 1.0 nM, $P < 0.05$). In conclusion, intravenous ANG II significantly inhibited the parasympathetic neurotransmission through AT_1 receptors. The failure of local losartan administration to nullify the inhibitory effect of ANG II on the stimulation-induced ACh release indicates that the site of this inhibitory action is likely at parasympathetic ganglia rather than at postganglionic vagal nerve terminals.

cardiac microdialysis; cats; losartan

ANG II HAS a variety of effects on the cardiovascular system (22): it acts on the vascular beds to increase peripheral vascular resistance and also on the adrenal cortex to cause volume retention. These direct effects of ANG II contribute to the maintenance of arterial pressure (AP). Aside from these direct effects, ANG II has been shown to modulate the sympathetic nervous system both centrally (7, 9) and peripherally (10). With respect to the sympathetic regulation in the heart, however, exogenous ANG II does not facilitate stimulation- and ischemia-induced norepinephrine release in the porcine left ventricle (18). Compared with a number of reports on the sympathetic system, only a few reports are available as to the effects of ANG II on the parasympathetic system. In 1982, Potter (23) demonstrated that ANG II (5–10 μg iv, body wt not reported) inhibited bradycardia induced by vagal stimulation in dogs. In that study, administration of ACh reduced the heart rate to an identical degree in the presence or absence of ANG II, suggesting that the inhibition of bradycardia by ANG II was attributable to the inhibition of the ACh release from the vagal nerve terminals. In contrast, Andrews et al. (3) reported that ANG II (500 ng/kg iv) did not inhibit bradycardia induced by vagal stimulation in ferrets. In a rat heart failure model, ANG II receptor subtype 1 (AT_1 receptor) antagonist losartan enhanced the bradycardic response to vagal stimulation (5). In pithed rats, an angiotensin-converting enzyme (ACE) inhibitor captopril also enhanced the bradycardic response to vagal stimulation (25, 26). In all of these studies, changes in the heart rate were used as a functional measurement of peripheral vagal function because of the difficulty in measuring the ACh release in the in vivo heart. Accordingly, whether ANG II affects the vagal control over the ventricle remains unknown. The aim of the present study was to examine the effect of ANG II on the vagal stimulation-induced ACh release in the left ventricular myocardium by measuring the interstitial ACh levels directly using a cardiac microdialysis technique (1, 13–15). We also explored the possible sites of action for the effect of ANG II on the stimulation-induced ACh release by administering losartan systemically from the femoral vein or locally through the dialysis fiber. Because ACh has a protective effect on the ischemic myocardium (12, 24, 29), elucidating the effect of ANG II on the ACh release in the ventricle would be helpful to understand the mechanism of ACE inhibitor or AT_1 receptor antagonist for the treatment of heart diseases (16, 17).

MATERIALS AND METHODS

Surgical Preparation

Animal care was provided in strict accordance with the *Guiding Principles for the Care and Use of Animals in the Field of Physiological Sciences* approved by the Physiological Society of Japan. All protocols were approved by the Animal Subject Committee of the National Cardiovascular Center. Twenty eight adult cats weighing from 1.9 to 4.9 kg were anesthetized using an intraperitoneal injection of pentobarbital sodium (30–35 mg/kg) and were then ventilated mechanically with room air mixed with oxygen. The depth of anesthesia was maintained by a continuous intravenous infusion of pentobarbital sodium (1–2 $mg \cdot kg^{-1} \cdot h^{-1}$) through a catheter inserted in the right femoral vein. Systemic AP was monitored by a catheter inserted in the right femoral artery. Heart rate was determined from an

Address for reprint requests and other correspondence: T. Kawada, Dept. of Cardiovascular Dynamics, National Cardiovascular Center Research Institute, 5-7-1 Fujishirodai, Suita, Osaka 565-8565, Japan (e-mail: torukawa@res.ncvc.go.jp).

The costs of publication of this article were defrayed in part by the payment of page charges. The article must therefore be hereby marked "*advertisement*" in accordance with 18 U.S.C. Section 1734 solely to indicate this fact.

electrocardiogram using a cardiotachometer. Esophageal temperature of the animal, measured using a thermometer (CTM-303; TERUMO), was maintained at ~37°C using a heating pad and a lamp. Both vagal nerves were exposed and sectioned bilaterally through a midline cervical incision. With the animal in the lateral position, we resected the left fifth and sixth ribs to approach the heart. After the incision of the pericardium, the heart was suspended in a pericardial cradle. Stainless steel wires were attached to the apex and the posterior wall of the left ventricle to pace the heart. Using a fine guiding needle, we implanted a dialysis probe transversely through the anterolateral free wall of the left ventricle. Next, we attached a pair of bipolar platinum electrodes to the cardiac end of each sectioned vagal nerve. The nerves and electrodes were covered in warmed mineral oil for insulation. We gave heparin sodium (100 U/kg) intravenously to prevent blood coagulation. At the end of the experiment, postmortem examination confirmed that the semipermeable membrane of the dialysis probe had been implanted in the left ventricular myocardium.

Dialysis Technique

The materials and properties of the dialysis probe have been described previously (1). Briefly, we designed a transverse dialysis probe in which a dialysis fiber of semipermeable membrane (13 mm length, 310 μm outer diameter, 200 μm inner diameter; PAN-1200, 50,000 mol wt cutoff; Asahi Chemical) was attached at both ends to polyethylene tubes (25 cm length, 500 μm outer diameter, 200 μm inner diameter). The dialysis probe was perfused at a rate of 2 μl/min with Ringer solution containing the cholinesterase inhibitor physostigmine (100 μM). Experimental protocols were started 2 h after implanting the dialysis probe when the ACh concentration in the dialysate reached a steady state. ACh concentrations in the dialysate were measured by an HPLC system with electrochemical detection (Eicom, Kyoto, Japan).

Figure 1 schematizes the three original protocols and two supplemental protocols utilized in the present study. The hatched rectangle indicates the baseline sampling, whereas the solid rectangles indicate the sampling during the 10-min vagal stimulation period (1 ms, 10 V, 20 Hz) in each protocol. The stimulus was set supramaximal to most easily delineate the possible effect of ANG II on myocardial interstitial ACh release. In all of the vagal stimulation periods, we paced the heart at 200 beats/min to avoid the difference in heart rate affecting the vagal stimulation-induced ACh release (14). For baseline sampling periods, we paced the heart at 200 beats/min when spontaneous heart rate was <200 beats/min.

Protocol 1 (n = 6). We examined the effects of intravenous administration of ANG II on vagal stimulation-induced myocardial ACh release. We collected a dialysate sample under baseline conditions. We then stimulated the vagal nerve and paced the heart for 10 min and collected a dialysate sample during the stimulation period

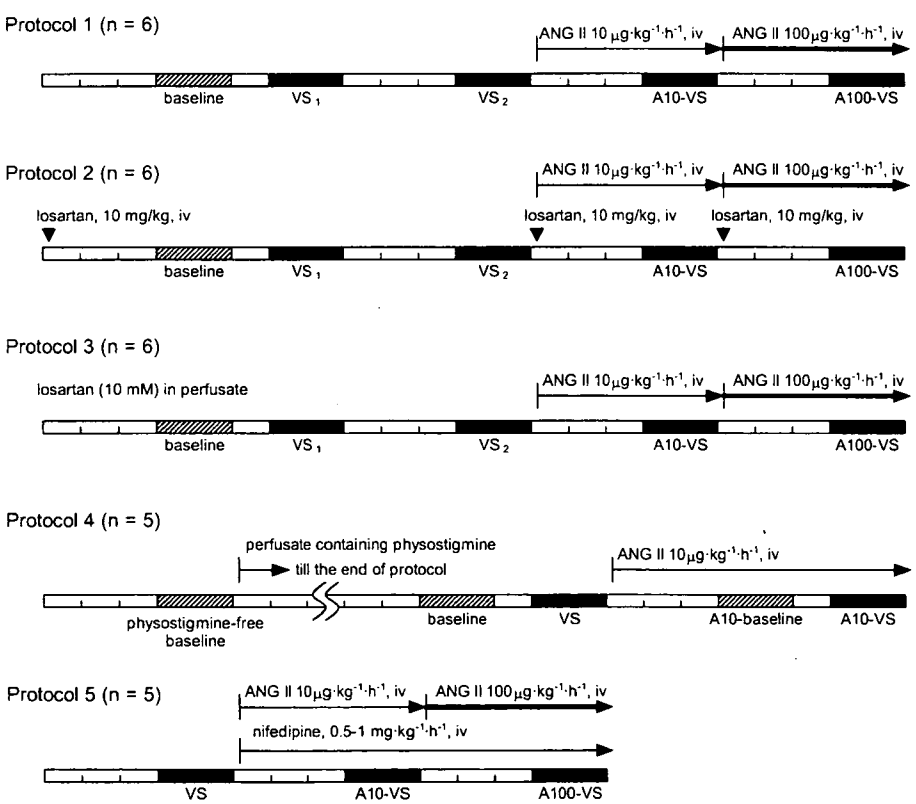

Fig. 1. Schematic representation of the protocols used in the present study. After implantation of the dialysis probe (2 h), we obtained a baseline dialysate sample (hatched rectangles) for 10 min. Thereafter, we obtained 4 dialysate samples during vagal stimulation with fixed-rate pacing for 10 min (filled rectangles) at intervening intervals of 15 min. In *protocols 1* through *3*, after obtaining 2 control trials (VS_1 and VS_2), we initiated intravenous administration of ANG II at 10 $\mu g \cdot kg^{-1} \cdot h^{-1}$ and waited for 15 min to obtain a dialysate sample during vagal stimulation with fixed-rate pacing (A10-VS). We then increased the dose of ANG II to 100 $\mu g \cdot kg^{-1} \cdot h^{-1}$ and waited for an additional 15 min before obtaining a dialysate sample during vagal stimulation with fixed-rate pacing (A100-VS). In *protocol 2*, the ANG II receptor subtype 1 blocker losartan was administered by bolus injection (10 mg/kg) before obtaining a baseline dialysate sample and also immediately before the beginning of each dose of ANG II administration (▼). In *protocol 3*, we administered losartan (10 mM) through the dialysis probe throughout the protocol. In *protocol 4*, we first collected a dialysate sample using perfusate free of physostigmine. We then replaced the perfusate with Ringer solution containing physostigmine and collected dialysate samples of baseline and vagal stimulation (VS). Approximately 15 min after the onset of iv ANG II administration at 10 $\mu g \cdot kg^{-1} \cdot h^{-1}$, we collected dialysate samples of baseline (A10-baseline) and vagal stimulation (A10-VS). In *protocol 5*, we collected dialysate samples during a control vagal stimulation (VS) and during the 2 doses of iv ANG II administration (A10-VS and A100-VS). The pressor effect of ANG II was counteracted by simultaneous iv infusion of the L-type Ca^{2+} channel blocker nifedipine.

(VS_1). After an intervening interval of 15 min, we repeated the 10-min vagal stimulation with fixed-rate pacing and collected another dialysate sample (VS_2). After performing these two control trials, we began intravenous administration of ANG II at 10 $\mu g \cdot kg^{-1} \cdot h^{-1}$. Approximately 15 min after the onset of the ANG II administration, we collected a dialysate sample (A10-VS) during 10-min vagal stimulation with fixed-rate pacing. We then increased the dose of ANG II at 100 $\mu g \cdot kg^{-1} \cdot h^{-1}$. Approximately 15 min after the onset of the higher-dose ANG II administration, we collected a final dialysate sample (A100-VS) during 10-min vagal stimulation with fixed-rate pacing.

Protocol 2 (n = 6). We examined whether the intravenous AT_1 receptor antagonist losartan would block the effects of ANG II on the vagal stimulation-induced myocardial ACh release. We infused losartan potassium intravenously at 10 mg/kg and waited for ~15 min. We then collected baseline, VS_1, and VS_2 samples with an intervening interval of 15 min, as described in *protocol 1*. Next, after an additional bolus injection of losartan potassium at 10 mg/kg, we began intravenous infusion of ANG II at 10 $\mu g \cdot kg^{-1} \cdot h^{-1}$. After ~15 min, we obtained a dialysate sample of A10-VS. Finally, after another bolus injection of losartan potassium at 10 mg/kg, we began intravenous infusion of ANG II at 100 $\mu g \cdot kg^{-1} \cdot h^{-1}$. After an additional 15 min, we obtained a dialysate sample of A100-VS.

Protocol 3 (n = 6). We examined whether local administration of losartan would block the effects of ANG II on the vagal stimulation-induced myocardial ACh release. We perfused the dialysis probe with Ringer solution containing 10 mM of losartan potassium. Taking into account the distribution across the semipermeable membrane, we administered losartan at a concentration >400 times higher than that for intravenous administration in *protocol 2*. Because local administrations of larger molecules such as ω-conotoxin GVIA (molecular weight 3037) and ω-conotoxin MVIIC (mol wt 2,749) were able to suppress vagal stimulation-induced ACh release in our previous study (15), it would be reasonable to assume that losartan potassium (mol wt 461) should have spread in the vicinity of the dialysis fiber, from which the dialysate was collected. Using the same procedures as described in *protocol 1*, we obtained dialysate samples for baseline, VS_1, VS_2, A10-VS, and A100-VS. A previous study indicated that ACh measured by cardiac microdialysis in the left ventricle mainly reflected ACh released from the postganglionic nerve terminals and not from the parasympathetic ganglia (1 and see DISCUSSION for details).

Protocol 4 (n = 5). To examine the effects of ANG II on the baseline ACh level, we performed an additional protocol where the baseline ACh level was measured during intravenous infusion of ANG II at 10 $\mu g \cdot kg^{-1} \cdot h^{-1}$ (A10-baseline). In this protocol, we also obtained a dialysate sample using the perfusate without the cholinesterase inhibitor physostigmine before the usual dialysate sampling using the perfusate containing physostigmine.

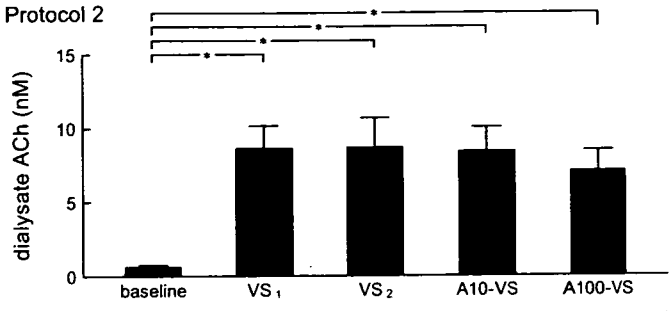

Fig. 3. Changes in dialysate ACh concentrations obtained from *protocol 2*. Vagal stimulation significantly increased the ACh levels. There was no significant difference in the ACh level among the 4 dialysate samples during vagal stimulation (VS_1, VS_2, A10-VS, and A100-VS). Values are presented as means and SE. *$P < 0.01$ by Tukey's test.

Protocol 5 (n = 5). To avoid the pressor effect of ANG II, we administered an L-type Ca^{2+} channel blocker nifedipine (0.5–2.0 $mg \cdot kg^{-1} \cdot h^{-1}$) simultaneously with ANG II and obtained dialysate samples for VS, A10-VS, and A100-VS. In a previous study, intravenous administration of an L-type Ca^{2+} channel blocker alone did not affect the vagal stimulation-induced myocardial ACh release significantly (15).

Statistical Analysis

All data are presented as mean ± SE values. In *protocols 1* through *3*, myocardial interstitial ACh levels were compared among baseline, VS_1, VS_2, A10-VS, and A100-VS samples using a repeated-measures ANOVA (8). When there was a significant difference, Tukey's test for all-pairwise comparisons was applied to identify the differences between any two of the samples. Differences were considered significant at $P < 0.05$. The mean AP value in the last 1 min of the 10-min vagal stimulation period was treated as the AP value during vagal stimulation. The AP data were compared using a repeated-measures ANOVA among baseline, during the two control stimulations (VS_1 and VS_2), and before and during vagal stimulation under the two different doses of intravenous ANG II administrations. When there was a significant difference, Dunnett's test for comparison against a single control was applied to identify differences from the baseline value. Differences were considered significant at $P < 0.05$. In

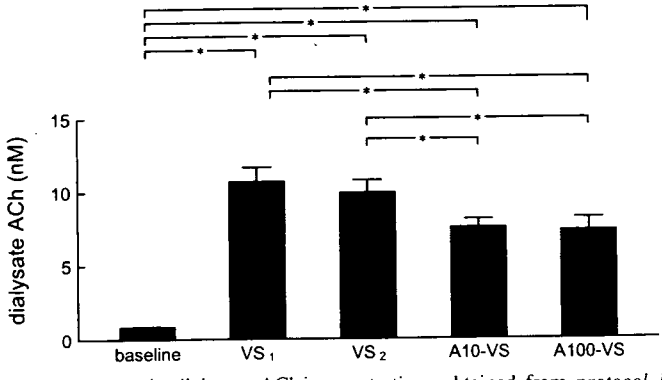

Fig. 2. Changes in dialysate ACh concentrations obtained from *protocol 1*. Vagal stimulation significantly increased the ACh levels. There was no significant difference in the ACh level between the 2 control trials (VS_1 and VS_2). The ACh level was significantly lower in A10-VS and A100-VS compared with that measured in VS_1 and VS_2. There was no significant difference in the ACh level between A10-VS and A100-VS. Values are presented as mean and SE. *$P < 0.01$ by Tukey's test.

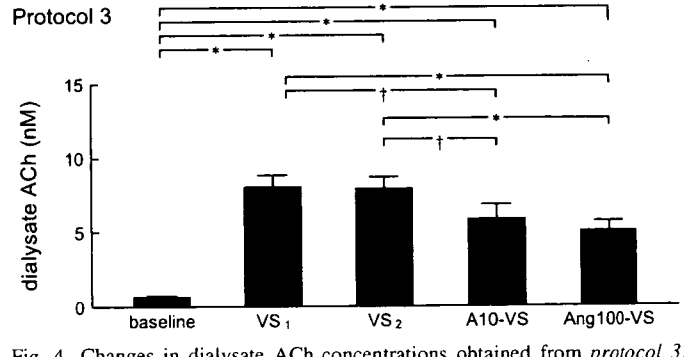

Fig. 4. Changes in dialysate ACh concentrations obtained from *protocol 3*. Vagal stimulation significantly increased the ACh levels. There was no significant difference in the ACh level between the 2 control trials (VS_1 and VS_2). The ACh level was significantly lower in A10-VS and A100-VS compared with that measured in VS_1 and VS_2. There was no significant difference in the ACh level between A10-VS and A100-VS. Values are presented as means and SE. †$P < 0.05$ and *$P < 0.01$ by Tukey's test.

Table 1. *Mean arterial pressure values before vagal stimulation and during the last 1 min of stimulation*

	Baseline	VS_1	VS_2	A10	A10-VS	A100	A100-VS
Protocol 1	102±11	93±17	91±17	132±9†	105±19	129±13†	105±21
Protocol 2	102±17	71±16*	69±16*	80±15	68±17*	86±19	72±18*
Protocol 3	102±13	100±17	92±17	139±11*	120±19	147±11*	122±21

Data are means ± SE obtained from baseline, two control trials (VS_1 and VS_2), before (A10) and during (A10-VS) vagal stimulation under iv administration of ANG II at 10 $\mu g \cdot kg^{-1} \cdot h^{-1}$, and before (A100) and during (A100-VS) vagal stimulation under iv administration of ANG II at 100 $\mu g \cdot kg^{-1} \cdot h^{-1}$. The heart was paced at 200 beats/min whenever vagal stimulation was applied. †$P < 0.05$ and *$P < 0.01$ from the respective baseline values by Dunnett's test.

protocol 4, the baseline ACh levels were compared before and during the ANG II administration using a paired *t*-test. The ACh levels during vagal stimulation were also compared before and during ANG II administration using a paired *t*-test. In *protocol 5*, the ACh levels and the mean AP values were compared among VS, A10-VS, and A100-VS using a repeated-measures ANOVA followed by Tukey's test.

RESULTS

In *protocol 1*, vagal stimulation significantly increased myocardial interstitial ACh levels (Fig. 2). There was no significant difference between two control trials with an intervening interval of 15 min [VS_1: 10.7 ± 1.0 (SE) nM and VS_2: 9.9 ± 0.9 (SE) nM]. Intravenous administration of ANG II at 10 $\mu g \cdot kg^{-1} \cdot h^{-1}$ significantly attenuated the vagal stimulation-induced ACh release (A10-VS: 7.5 ± 0.6 nM) to ~71% of VS_1. Although the intravenous administration of ANG II at 100 $\mu g \cdot kg^{-1} \cdot h^{-1}$ also significantly attenuated the vagal stimulation-induced ACh release (A100-VS: 7.3 ± 0.9 nM) to ~68% of VS_1, the ACh levels were not different from those of A10-VS.

In *protocol 2*, vagal stimulation significantly increased myocardial interstitial ACh levels under control stimulations (VS_1: 8.6 ± 1.5 nM and VS_2: 8.7 ± 2.0 nM; Fig. 3). With a pretreatment of intravenous losartan, intravenous ANG II was unable to suppress the vagal stimulation-induced ACh release (A10-VS: 8.4 ± 1.7 nM and A100-VS: 7.1 ± 1.4 nM). Although the mean level of ACh tended to be lower in A100-VS compared with VS_1 or VS_2, the differences were not statistically significant.

In *protocol 3*, vagal stimulation significantly increased myocardial interstitial ACh levels under control stimulations (VS_1: 8.0 ± 0.8 nM and VS_2: 7.9 ± 0.8 nM; Fig. 4). Intravenous ANG II at either 10 $\mu g \cdot kg^{-1} \cdot h^{-1}$ or 100 $\mu g \cdot kg^{-1} \cdot h^{-1}$ significantly suppressed the vagal stimulation-induced ACh release to ~72% (A10-VS: 5.8 ± 1.0 nM) and 62% (A100-VS: 5.0 ± 0.7 nM of that seen in VS_1), respectively.

In *protocol 1*, the AP values before the vagal stimulation during the intravenous ANG II administrations (A10 and A100) were significantly higher than the baseline AP value (Table 1). The AP values during vagal stimulation (VS_1, VS_2, A10-VS, and A100-VS) were not different from the baseline AP value. In *protocol 2*, the AP value before the first administration of losartan was 126 ± 14 mmHg. The AP values before the vagal stimulation during the intravenous ANG II administrations (A10 and A100) were not significantly different from the baseline AP value. The AP values during vagal stimulation (VS_1, VS_2, A10-VS, and A100-VS) were significantly lower than the baseline AP value. In *protocol 3*, the AP values before vagal stimulation during the intravenous ANG II administrations (A10 and A100) were significantly higher than the baseline AP value. The AP values during vagal stimulation (VS_1, VS_2, A10-VS, and A100-VS) did not differ statistically from the baseline AP value.

Figure 5 illustrates typical chromatograms obtained from one animal in *protocol 4*. The baseline ACh level was below the limit of determination (0.5 nM) when the perfusate did not contain physostigmine. Approximately 1 h after replacing the perfusate with Ringer solution containing physostigmine, the baseline ACh level was above the limit of determination. As shown in Table 2, vagal stimulation significantly increased the ACh level (VS). The intravenous administration of ANG II did not affect the baseline ACh level (A10-basline) but significantly attenuated the ACh level during vagal stimulation (A10-VS).

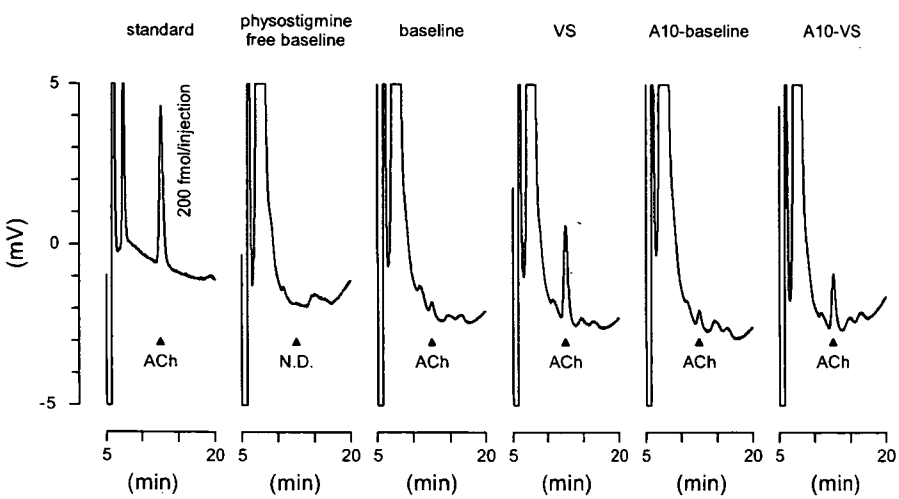

Fig. 5. Typical chromatograms for the ACh measurements obtained from *protocol 4*. ACh was less than the limit of determination when perfusate did not contain physostigmine (physostigmine-free baseline). The baseline ACh level was above the limit of determination when perfusate contained 100 μM physostigmine. (This perfusate was usually used for the ACh measurements.) Vagal stimulation increased the ACh level (VS). The administration of ANG II at 10 $\mu g \cdot kg^{-1} \cdot h^{-1}$ did not affect baseline ACh level (A10-baseline) but significantly attenuated the vagal stimulation-induced ACh release (A10-VS). See Table 2 for pooled data of ACh levels. ND, not detected.

Table 2. *Mean arterial pressure values and ACh concentrations obtained in protocol 4*

	Physostigmine-free Baseline	Baseline	VS	A10-Baseline	A10-VS
ACh, nM	Not detected	1.6±0.4	10.6±2.4	1.7±0.5	7.8±2.1*
Mean arterial pressure, mmHg	111±11	109±12	103±6	148±3*	118±6

Data are means ± SE obtained from physostigmine-free baseline, baseline, control vagal stimulation (VS), and baseline (A10-baseline) and vagal stimulation (A10-VS) under iv administration of ANG II at 10 $\mu g \cdot kg^{-1} \cdot h^{-1}$. There was no significant difference in the ACh level between baseline and A10-baseline by a paired-*t*-test. The ACh level was significantly lower in A10-VS than in VS by a paired-*t*-test. Mean arterial pressure was significantly higher in A10-baseline compared with the physostigmine-free baseline value by Dunnett's test. *$P < 0.01$.

In *protocol 5*, the pressor effect of ANG II was counteracted by the simultaneous intravenous infusion of nifedipine (Table 3). Under this condition, the intravenous administration of ANG II significantly attenuated the stimulation-induced ACh level to ~83% (A10-VS) and 72% (A100-VS) of that seen in VS.

DISCUSSION

The present study demonstrated that intravenous ANG II significantly inhibited the vagal stimulation-induced myocardial interstitial ACh release in the left ventricle in anesthetized cats. Intravenous administration of losartan abolished the inhibitory effect of ANG II on the stimulation-induced ACh release, suggesting that the inhibitory action of ANG II was mediated by AT_1 receptors.

Inhibitory Effect of ANG II on Myocardial Interstitial ACh Release

Only a few reports have focused on the modulatory effects of ANG II on the parasympathetic nervous system (3, 5, 25, 26), all of which have used the heart rate reduction in response to vagal stimulation as a functional measurement to assess the peripheral vagal function. Although ANG II has been shown to inhibit the ACh release in the rat entorhinal cortex in vitro (4), the direct evidence for the inhibitory effect of ANG II on the ACh release in the peripheral vagal neurotransmission in vivo has been lacking. The present study demonstrated that intravenous ANG II inhibited the vagal nerve stimulation-induced ACh release in the left ventricle in vivo (Fig. 2). As for the sympathetic system in the heart, Lameris et al. (18) have previously demonstrated that ANG II does not affect the sympathetic nerve stimulation-induced norepinephrine release. The insignificant effect of ANG II on the sympathetic neurotransmission and the inhibitory effect of ANG II on the parasympathetic neurotransmission may provide the basis for a study by Takata et al. (26) in which ACE inhibitor enhanced cardiac vagal but not sympathetic neurotransmission.

Table 3. *Mean arterial pressure values and ACh concentrations obtained in protocol 5*

	VS	A10-VS	A100-VS
ACh, nM	12.7±1.1	10.6±1.1†	9.2±1.5*
Mean arterial pressure, mmHg	83.4±12.2	68.4±6.3	70.4±9.5

Data are means ± SE from a control vagal stimulation trial (VS), during vagal stimulation under iv administration of ANG II at 10 $\mu g \cdot kg^{-1} \cdot h^{-1}$ (A10-VS) and during vagal stimulation under iv administration of ANG II at 100 $\mu g \cdot kg^{-1} \cdot h^{-1}$ (A100-VS). The heart was paced at 200 beats/min during vagal stimulation. In this protocol, the pressor effect of ANG II was counteracted by simultaneous iv administration of the L-type Ca^{2+} channel blocker nifedipine (0.5–2 $mg \cdot kg^{-1} \cdot h^{-1}$). †$P < 0.05$ and *$P < 0.01$ from the VS group by Tukey's test. There was no significant difference between A10-VS and A100-VS in the ACh level. There were no significant differences in mean arterial pressure among the three trials.

An increased activity of the renin-angiotensin system is common in chronic heart failure and has been considered to be a stimulus for aggravation of the disease. Inhibition of the renin-angiotensin system by ACE inhibitors or by AT_1 receptor blockers can prevent the ventricular remodeling and improve the survival rate (16, 17), suggesting that ANG II is indeed involved in the aggravation of heart failure. ACh, on the other hand, can exert a cardioprotective effect against myocardial ischemia in several experimental settings (12, 24, 29). If ANG II inhibits the peripheral vagal neurotransmission, blockade of ANG II would increase the vagal effect on the heart. Actually, Du et al. (5) demonstrated that losartan enhanced bradycardia induced by vagal stimulation in rats with chronic myocardial infarction. In that study, however, the ventricular effect of vagal stimulation was not assessed. The results of the present study indicate that ANG II inhibited the vagal neurotransmission in the ventricle. Blockade of ANG II is therefore expected to increase the vagal effect on the ventricular myocardium when the vagal outflow from the central nervous system is unchanged. Although no literatures appear to be available as to the chronic effect of ACh on the prognosis of heart failure, electrical vagal stimulation was able to improve the survival rate of chronic heart failure in rats (19). In that study, the magnitude of the vagal stimulation was such that the heart rate decreased only by 20–30 beats/min in rats, suggesting that a modest increase in vagal tone would be sufficient to produce a cardioprotective effect. It is plausible that blockade of ANG II yields beneficial effects on chronic heart failure not only by antagonizing the sympathetic effects but also by enhancing the vagal effects on the ventricle.

Vagal stimulation was able to reduce the left ventricular contractility as assessed by end-systolic elastance only when sympathetic stimulation coexisted (20), suggesting that the effect of vagal stimulation on ventricular contractility would be secondary to sympathoinhibition. Accordingly, contribution of the inhibitory effect of ANG II on the stimulation-induced ACh release to the physiological regulation of ventricular contractility might be marginal. We think that the finding is important as a peripheral mechanism of vagal withdrawal in heart diseases accompanying the activation of the renin-angiotensin system.

Possible Site of the Inhibitory Action of ANG II on ACh Release

In *protocol 3*, we examined whether local administration of losartan was able to nullify the inhibitory effect of ANG II on the vagal stimulation-induced ACh release. The utility of local administration of pharmacological agents through the dialysis fiber has been confirmed previously. As an example, local administration the Na^+ channel inhibitor tetrodotoxin through the dialysis fiber completely blocked the nerve stimulation-induced ACh release (14). With respect to the source for ACh, intravenous administration of the nicotinic antagonist hexamethonium bromide completely blocked the stimulation-induced ACh release, whereas local administration of hexamethonium bromide did not, suggesting the lack of parasympathetic ganglia in the vicinity of dialysis fiber (1). In support of our interpretation, a neuroanatomic finding indicates that three ganglia, away from the left anterior free wall targeted by the dialysis probe, provide the major source of left ventricular postganglionic innervation in cats (11). Therefore, the myocardial interstitial ACh measured by cardiac microdialysis in the left ventricle mainly reflects the ACh release from the postganglionic vagal nerve terminals. The results of *protocol 3* indicate that losartan spread around the postganglionic vagal nerve terminals failed to abolish the inhibitory effect of ANG II on the stimulation-induced ACh release. Because intravenous administration of losartan was able to abolish the inhibitory effect of ANG II on the stimulation-induced ACh release (*protocol 2*), the site of this inhibitory action is likely at parasympathetic ganglia rather than at postganglionic vagal nerve terminals. The fact that AT_1 receptors are rich in parasympathetic ganglia (2) would support our interpretation.

ANG II has a direct vasoconstrictive effect on the coronary artery (30). At the same time, however, the intravenous administration of ANG II tended to increase mean AP during vagal stimulation by ~15 mmHg in *protocol 1* (Table 1). Although it was statistically insignificant, if this increase in mean AP increased cardiac oxygen demand, the coronary blood flow might have been increased (27), resulting in an increased rate of washout in the myocardial tissue. The possibility cannot be ruled out that such a washout mechanism contributed to the reduction of stimulation-induced ACh release during ANG II administration. However, the baseline ACh level was not decreased by ANG II in *protocol 4*, suggesting that the washout rate did not increase significantly. In addition, even when the pressor effect of ANG II was counteracted by nifedipine, ANG II was still able to inhibit the vagal stimulation-induced ACh release in *protocol 5*. Therefore, we think that the change in washout rate was not a principal mechanism for the reduction of stimulation-induced ACh release by ANG II.

The mechanisms for the baseline ACh release under the vagotomized condition were not identified in the present study. In the motor nerve terminals, a so-called nonquantal release of ACh is documented, which is independent of nerve activity (6). Incorporation of the vesicular transport system in the membrane of the nerve terminals during an exocytosis process is considered to be responsible for the mechanism of nonquantal ACh release. A similar mechanism might contribute to the baseline ACh release in the vagal nerve terminals.

Several limitations need to be addressed. First, the dose of ANG II might have increased the plasma ANG II concentration beyond the physiological range. In this regard, the observed effect might be rather pharmacological or pathological than physiological. Nevertheless, because there are local synthesis and degradation of ANG II in the heart (21, 28), the inhibition of ACh release by ANG II could operate locally in the heart. Second, whether ANG II inhibited the ACh release from the preganglionic nerve terminals or it suppressed the excitability of the postganglionic nerve fibers to ACh was not identified in the present study. Third, the involvement of ANG II receptor subtype 2 (AT_2 receptor) in the modulation of peripheral parasympathetic neurotransmission was not examined in the present study because intravenous losartan was able to abolish the inhibitory effect of ANG II on the stimulation-induced ACh release. However, if coactivation of AT_1 and AT_2 receptors is required for the inhibitory effect of ANG II, blockade of AT_2 receptors would also abolish the inhibitory effect. Forth, we tested just one level of vagal stimulation. Whether the effect of ANG II on the stimulation-induced ACh release depends on the vagal stimulation intensity remains to be resolved.

In conclusion, intravenous ANG II reduced the vagal nerve stimulation-induced ACh release in the left ventricle. Intravenous losartan abolished the inhibitory effect of ANG II on the stimulation-induced ACh release, suggesting that this inhibition was mediated by AT_1 receptors. Because local administration of losartan via dialysis fiber was unable to nullify the inhibitory effect of ANG II on the stimulation-induced ACh release, the site of this inhibitory action is likely parasympathetic ganglia. The present results imply that the beneficial effects of ACE inhibitors and AT_1 receptor antagonists in the treatment of heart diseases may include not only the suppression of sympathetic activity but also the enhancement of vagal activity to the ventricle.

GRANTS

This study was supported by a Health and Labour Sciences Research Grant for Research on Advanced Medical Technology, a Health and Labour Sciences Research Grant for Research on Medical Devices for Analyzing, Supporting, and Substituting the Function of Human Body, and Health and Labour Sciences Research Grant H18-Iryo-Ippan-023 from the Ministry of Health, Labour, and Welfare of Japan.

REFERENCES

1. **Akiyama T, Yamazaki T, Ninomiya I.** In vivo detection of endogenous acetylcholine release in cat ventricles. *Am J Physiol Heart Circ Physiol* 266: H854–H860, 1994.
2. **Allen AM, Zhuo J, Mendelsohn FA.** Localization and function of angiotensin AT_1 receptors. *Am J Hypertens* 13: 31S–38S, 2000.
3. **Andrews PL, Dutia MB, Harris PJ.** Angiotensin II does not inhibit vagally-induced bradycardia or gastric contractions in the anaesthetized ferret. *Br J Pharmacol* 82: 833–837, 1984.
4. **Barnes JM, Barnes NM, Costall B, Horovitz ZP, Naylor RJ.** Angiotensin II inhibits the release of [^{3}H]acetylcholine from rat entorhinal cortex in vitro. *Brain Res* 491: 136–143, 1989.
5. **Du XJ, Cox HS, Dart AM, Esler MD.** Depression of efferent parasympathetic control of heart rate in rats with myocardial infarction: effect of losartan. *J Cardiovasc Pharmacol* 31: 937–944, 1998.
6. **Edwards C, Doležal V, Tuček S, Zemková H, Vyskočil F.** Is an acetylcholine transport system responsible for nonquantal release of acetylcholine at the rodent myoneural junction? *Proc Natl Acad Sci USA* 82: 3354–3518, 1985.
7. **Gao L, Wang W, Li Y, Schultz HD, Liu D, Cornish KG, Zucker IH.** Sympathoexcitation by central ANG II: roles for AT_1 receptor upregulation and NAD(P)H oxidase in RVLM. *Am J Physiol Heart Circ Physiol* 288: H2271–H2279, 2005.
8. **Glantz SA.** *Primer of Biostatistics* (5th ed.). New York: McGraw-Hill, 2002.

9. **Hirooka Y, Head GA, Potts PD, Godwin SJ, Bendle RD, Dampney RA.** Medullary neurons activated by angiotensin II in the conscious rabbit. *Hypertension* 27: 287–296, 1996.
10. **Hughes J, Roth RH.** Evidence that angiotensin enhances transmitter release during sympathetic nerve stimulation. *Br J Pharmacol* 41: 239–255, 1971.
11. **Johnson TA, Gray AL, Lauenstein JM, Newton SS, Massari VJ.** Parasympathetic control of the heart. *I.* An interventriculo-septal ganglion is the major source of the vagal intracardiac innervation of the ventricles. *J Appl Physiol* 96: 2265–2272, 2004.
12. **Kakinuma Y, Ando M, Kuwabara M, Katare RG, Okudela K, Kobayashi M, Sato T.** Acetylcholine from vagal stimulation protects cardiomyocytes against ischemia and hypoxia involving additive non-hypoxic induction of HIF-1alpha. *FEBS Lett* 579: 2111–2118, 2005.
13. **Kawada T, Yamazaki T, Akiyama T, Sato T, Shishido T, Inagaki M, Takaki H, Sugimachi M, Sunagawa K.** Differential acetylcholine release mechanisms in the ischemic and non-ischemic myocardium. *J Mol Cell Cardiol* 32: 405–414, 2000.
14. **Kawada T, Yamazaki T, Akiyama T, Shishido T, Inagaki M, Uemura K, Miyamoto T, Sugimachi M, Takaki H, Sunagawa K.** In vivo assessment of acetylcholine-releasing function at cardiac vagal nerve terminals. *Am J Physiol Heart Circ Physiol* 281: H139–H145, 2001.
15. **Kawada T, Yamazaki T, Akiyama T, Uemura K, Kamiya A, Shishido T, Mori H, Sugimachi M.** Effects of Ca^{2+} channel antagonists on nerve stimulation-induced and ischemia-induced myocardial interstitial acetylcholine release in cats. *Am J Physiol Heart Circ Physiol* 291: H2187–H2191, 2006.
16. **Konstam MA, Neaton JD, Poole-Wilson PA, Pitt B, Segal R, Sharma D, Dasbach EJ, Carides GW, Dickstein K, Riegger G, Camm AJ, Martinez FA, Bradstreet DC, Ikeda LS, Santoro EP, investigators ELITEII.** Comparison of losartan and captopril on heart failure-related outcomes and symptoms from the losartan heart failure survival study (ELITE II). *Am Heart J* 150: 123–131, 2005.
17. **Konstam MA, Rousseau MF, Kronenberg MW, Udelson JE, Melin J, Stewart D, Dolan N, Edens TR, Ahn S, Kinan D, Howe DM, Kilcoyne L, Metherall J, Benedict C, Yusuf S, Pouleur H, investigators SOLVD.** Effects of the angiotensin converting enzyme inhibitor enalapril on the long-term progression of left ventricular dysfunction in patients with heart failure. *Circulation* 86: 431–438, 1992.
18. **Lameris TW, de Zeeuw S, Duncker DJ, Alberts G, Boomsma F, Verdouw PD, van den Meiracker AH.** Exogenous angiotensin II does not facilitate norepinephrine release in the heart. *Hypertension* 40: 491–497, 2002.
19. **Li M, Zheng C, Sato T, Kawada T, Sugimachi M, Sunagawa K.** Vagal nerve stimulation markedly improves long-term survival after chronic heart failure in rats. *Circulation* 109: 120–124, 2004.
20. **Nakayama Y, Miyano H, Shishido T, Inagaki M, Kawada T, Sugimachi M, Sunagawa K.** Heart rate-independent vagal effect on end-systolic elastance of the canine left ventricle under various levels of sympathetic tone. *Circulation* 104: 2277–2279, 2001.
21. **Paul M, Mehr AP, Kreutz R.** Physiology of local renin-angiotensin systems. *Physiol Rev* 86: 747–803, 2006.
22. **Peach MJ.** Renin-angiotensin system: Biochemistry and mechanisms of action. *Physiol Rev* 57: 313–370, 1977.
23. **Potter EK.** Angiotensin inhibits action of vagus nerve at the heart. *Br J Pharmacol* 75: 9–11, 1982.
24. **Qin Q, Downey JM, Cohen MV.** Acetylcholine but not adenosine triggers preconditioning through PI3-kinase and a tyrosine kinase. *Am J Physiol Heart Circ Physiol* 284: H727–H734, 2003.
25. **Rechtman M, Majewski H.** A facilitatory effect of anti-angiotensin drugs on vagal bradycardia in the pithed rat and guinea-pig. *Br J Pharmacol* 110: 289–296, 1993.
26. **Takata Y, Arai T, Suzuki S, Kurihara J, Uezono T, Okubo Y, Kato H.** Captopril enhances cardiac vagal but not sympathetic neurotransmission in pithed rats. *J Pharmacol Sci* 95: 390–393, 2004.
27. **Tune JD, Gorman MW, Feigl EO.** Matching coronary blood flow to myocardial oxygen consumption. *J Appl Physiol* 97: 404–415, 2004.
28. **van Kats JP, Danser AH, van Meegen JR, Sassen LM, Verdouw PD, Schalekamp MA.** Angiotensin production by the heart. A quantitative study in pigs with the use of radiolabeled angiotensin infusions. *Circulation* 98: 73–81, 1998.
29. **Yao Z, Gross GJ.** Acetylcholine mimics ischemic preconditioning via a glibenclamide-sensitive mechanism in dogs. *Am J Physiol Heart Circ Physiol* 264: H2221–H2225, 1993.
30. **Zhang C, Knudson JD, Setty S, Araiza A, Dincer üD, Kuo L, Tune JD.** Coronary arteriolar vasoconstriction to angiotensin II is augmented in prediabetic metabolic syndrome via activation of AT_1 receptors. *Am J Physiol Heart Circ Physiol* 288: H2154–H2162, 2005.

IEICE TRANS. FUNDAMENTALS, VOL.E90–A, NO.6 JUNE 2007

LETTER

A Combined Coding and Modulation to Support Both Coherent and Non-coherent Ultra-Wideband Receivers

Tomoko MATSUMOTO[†a)], *Student Member and* Ryuji KOHNO[†], *Fellow*

SUMMARY This letter proposes a simple combined coding and modulation based on super-orthogonal convolutional codes (SOCs) in order to support both coherent and non-coherent ultra-wideband (UWB) receivers. In the proposed scheme, the coherent receivers obtain a coding gain as large as the SOC while simultaneously supporting non-coherent receivers. In addition, their performance can be freely adapted by changing the encoder constraint length and the number of PPM slots according to its application. Thus, the proposal enables a more flexible system design for low data-rate UWB systems.

key words: *ultra-wideband, low data-rate wireless personal area networks, super-orthogonal convolutional codes*

1. Introduction

Low data-rate ultra-wideband (LDR-UWB) is a low cost wireless technology, which has been widely studied recently and is expected to serve as a core physical layer technology for sensor networks. So far, in [1], [2], a number of receiver structures have been proposed for coherent detectors and non-coherent detectors individually which have differing signaling scheme, meaning that there does not exist any communications between the two types of nodes.

However, in order to meet the needs to use LDR-UWB more widely, the identical signaling scheme should be applied for coherent and non-coherent nodes which enables more flexible system design. In order for coherent and non-coherent nodes to receive the same transmitted signal, the modulation scheme should be carefully selected. Recently, the standard of IEEE 802.15.4a [3] applied a modulation scheme that combines pulse-position modulation (PPM) and bi-phase shift-keying (BPSK) so that the performance of the coherent nodes improves while simultaneously supporting the non-coherent nodes. This modulation scheme is effectively combined with a half-rate systematic convolutional code with constraint length three [3]. However, this coding scheme can be applied only with a fixed encoder constraint length.

In this letter, we propose a compatible combined coding and modulation which supports both coherent and non-coherent receivers. The design criteria for the proposed scheme is threefold: 1) the amount of information bits to be received is the same for coherent and non-coherent receivers; 2) the receiver should be low-complexity, therefore decoder with a relatively small number of states is designed; 3) the performance of the coherent receivers does not deteriorate due to the non-coherent receivers.

This letter presents a practical solution that meets this design criteria based on super-orthogonal codes (SOCs) [4]–[8]. The performance of the proposed method can be freely adapted according to its use by changing the number of PPM slots and the encoder constraint length; thereby enabling a flexible system design for LDR-UWB systems.

2. System Description

Consider a wireless network in which two types of receivers exist, i.e., coherent receivers and non-coherent energy detection receivers (simply referred to as *non-coherent receiver* in this letter). The transmitter has no knowledge of the type of destination receiver. Therefore, the transmit signal should be designed in order to support the two types of receivers.

The modulation scheme employed in this letter is a combination of BPSK and M-ary PPM (MPPM)*. It is known that with coherent detection BPSK performs better than PPM because of the larger Euclidean distance [9]. On the other hand, the non-coherent receivers are unable to demodulate the BPSK symbols since it requires the knowledge of the polarity of the signals. This leads us to believe that a combination of PPM and BPSK should be used as the modulation scheme so that the performance of the coherent receivers improves while simultaneously supporting the non-coherent receivers.

Let $\boldsymbol{u} = [u_0, \ldots, u_{N_b-1}] \in \{0, 1\}$ define the information bits where N_b is the number of bits in a packet. The information bits are convolutional coded and mapped to both the polarity $\boldsymbol{d} = [d_0, \ldots, d_{N_b-1}] \in \{\pm 1\}$ and positions $\boldsymbol{\delta} = [\delta_0, \ldots, \delta_{N_b-1}] \in \{0, 1, \ldots, M-1\}$. (the mapping rule will be described in Sect. 3.) For simplicity, this letter assumes single-user scenario and thus, multiple access scheme such as time-hopping is not considered. The synchronization between transmitter and receiver is assumed to be perfectly established prior to data transmission. Then, the received signal is represented as

$$r(t) = \sum_{n=0}^{N_b-1} d_n \sum_{l=0}^{L_p-1} \alpha_l p(t - \delta_n T_{ppm} - nT_b - \tau_l) + \nu(t), \quad (1)$$

*In Ref. [10], this modulation scheme is referred to as 'biorthogonal pulse position modulation.'

Manuscript received September 11, 2006.
Manuscript revised January 22, 2007.
Final manuscript received March 5, 2007.

[†]The authors are with the Division of Physics, Electrical and Computer Engineering, Graduate School of Engineering, Yokohama National University, Yokohama-shi, 240-8501 Japan.
a) E-mail: tomoko@kohnolab.dnj.ynu.ac.jp

DOI: 10.1093/ietfec/e90–a.6.1252

where $p(t)$ is a transmit pulse shape which is a impulse response of a root cosine filter with roll-off factor $\beta = 0.6$. The bit duration is denoted by T_b which is divided into M PPM slots each with duration $T_{ppm} = T_b/M$. The PPM duration is large enough so that the different PPM symbols are orthogonal to each other. The number of multipath components is denoted by L_p. The amplitude and delay of each path are denoted by α_l and τ_l, respectively. The complex additive white Gaussian noise (AWGN) with two-sided power spectral density $N_0/2$ is denoted by $v(t)$. The received signal goes through the received root cosine filter yielding $\tilde{r}(t) = r(t) * p(-t)$.

2.1 Non-coherent Receiver

The non-coherent receivers collect the signal energy by using a square-law device. The non-coherent receivers are simple in the sense that precise synchronization and channel estimation are not needed. The decision variables for the nth bit, denoted as $y_n^{NC} = [y_n^{NC}(0), \ldots, y_n^{NC}(M-1)]$, are given as follows:

$$y_n^{NC}(m) = \int_0^{T_i} \left| \tilde{r}(t + mT_{ppm} + nT_b) \right|^2 dt, \; 0 \le m < M, \qquad (2)$$

where T_i $(0 < T_i \le T_{ppm})$ is the integration duration which is selected according to the delay spread of the channel [11]. From Eq. (2), the receivers only detect the pulse-position; they do not attempt to estimate the polarity.

2.2 Coherent Receiver

In the case of the coherent receivers, maximum-ratio combining RAKE is employed to exploit multipath diversity. The receivers assume the perfect channel estimation. First, the received filter output $\tilde{r}(t)$ is sampled with a sampling interval Δt. Out of the sampled signals, L samples are chosen by their magnitudes as RAKE branches. Let $\{\theta_l\}_{l=0}^{L-1}$ and $\{\rho_l\}_{l=0}^{L-1}$ denote the path index and the estimation of the amplitude, respectively, of the selected largest L paths. The decision variables for the nth bit, $y_n^C = [y_n^C(0), \ldots, y_n^C(M-1)]$, are computed as

$$y_n^C(m) = \sum_{l=0}^{L-1} \Re\left[\rho_l^* y_{n,l}(m)\right], \; 0 \le m < M, \qquad (3)$$

where $\Re[z]$ denotes the real-part of complex number z, $y_{n,l}(m) := \tilde{r}(mT_{ppm} + nT_b + \theta_l \Delta t)$. As opposed to the non-coherent receivers, the coherent receivers estimate the pulse-position as well as the polarity of the transmitted pulses.

3. Proposed Combined Coding and Modulation

This section describes the mapping rule of the information bits $\boldsymbol{u}$ into the polarity $\boldsymbol{d}$ and position $\boldsymbol{\delta}$ of the transmit pulses. As mentioned earlier, the mapping rule should satisfy the following conditions: 1) the amount of information bits to be received is the same for coherent and non-coherent receivers; 2) the decoder has a relatively small number of states; 3) the performance of the coherent receivers does not deteriorate due to the non-coherent receivers.

In what follows, we describe a simple coding and modulation that satisfies the above three conditions based on SOCs [4]. First, we introduce the SOCs as well as orthogonal convolutional codes (OCs) and then show the application of these codes to the proposed scheme.

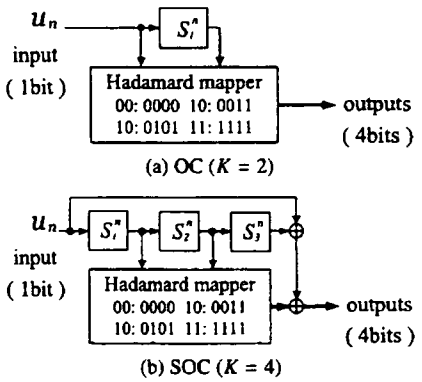

Fig. 1 Examples of encoder structure of (a) OC and (b) SOC.

3.1 The Review of OCs and SOCs

Figure 1 shows the encoder structure for the OC with constraint length $K = 2$ and SOC with $K = 4$, respectively. Each encoder has a K bit shift register and a Hadamard encoder [13]. The encoder state at time n is denoted by $[S_1^n, \ldots, S_{K-1}^n] \in \{0, 1\}$, where $S_i^0 = 0$ $(0 \le i < K)$.

In the OC encoder in Fig. 1(a), the input at time n u_n and the previous input $S_1^n (= u_{n-1})$ are inputted to the Hadamard encoder which works by selecting one of the rows of a 4×4 Hadamard matrix. Consequently, each of the encoder outputs corresponds to one of the rows in the Hadamard matrix. The minimum free distance of the OC is increased by utilizing the orthogonality between the codewords. Since decoding is required to detect the sequence being transmitted, the OC can be used with non-coherent detection [4].

The SOC was introduced by modifying OC. In this case, the inner two bits out of four bits shift register are mapped to one of the rows of a 4×4 Hadamard matrix. Then, the two outer bits are added to the selected Hadamard sequence by modulo-2 addition. The codewords are one of the rows of the Hadamard matrix as well as its complementary matrix, i.e., the SOC has bi-orthogonal codewords. This increases its minimum free distance more than that of the OC. In this case, since one Hadamard sequence and the complementary sequence need to be distinguished, coherent detection is necessary.

Note that the outputs of the Hadamard encoder in Fig. 1(b) can be viewed as the outputs of the OC encoder with $K = 2$. In other words, an OC encoder with constraint length $(K-2)$ is used in the SOC encoder of constraint length K. Thus, OC can be considered to be a subset of SOC. By

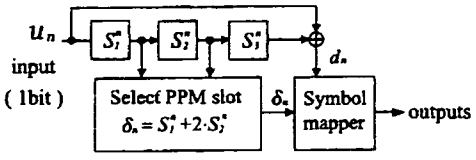

Fig. 2 Proposed combined coding and modulation ($K = 4, M = 4$).

exploiting this property, a novel coding scheme is presented in the following subsection.

3.2 Mapping Information Bits to BPSK/MPPM Symbols

Figure 2 shows the encoder for the proposed combined coding and modulation scheme with $K = 4$. In the proposed scheme, the inner $(K-2)$ bit in the shift register are used to select one PPM slot from $M = 2^{K-2}$ slots as

$$\delta_n = \sum_{i=1}^{K-2} S_i^n \cdot 2^{i-1}. \tag{4}$$

Then, the two outer bits are added by modulo-2 addition; this determines the polarity of the transmitted pulses.

$$a_n = u_n \oplus S_{K-1}^n, \tag{5}$$

$$d_n = \begin{cases} 1 & (a_n = 0) \\ -1 & (a_n = 1). \end{cases} \tag{6}$$

In this mapping procedure, the coherent receivers obtain a coding gain as large as that of the SOC, since it has bi-orthogonal codewords as in SOC. The only difference is that PPM is used in place of the Hadamard sequences to construct $2M$ bi-orthogonal codewords. The same concept was used in [8] using orthogonal pulse shapes.

On the other hand, the non-coherent receivers receive only M codewords out of $2M$ codewords since it can not see the polarity. However, the non-coherent receivers can successfully decode the transmitted codewords by using the OC decoder having constraint length $(K-2)$. Note that the orthogonal (non-overlapped) PPM signaling is the only method for the non-coherent receivers to detect a set of M orthogonal codewords, in other words, obtain a coding gain.

It should be also noted that the proposed scheme with $K = 3$ is equivalent to the inner code of [3] (i.e., combined BPSK/2PPM and a half-rate systematic convolutional code).

3.3 Viterbi Decoding

The decoding for the proposed code is performed by using maximum-likelihood (ML) Viterbi decoding.

3.3.1 Non-coherent Receiver

The non-coherent receivers decode the received codewords by using a OC decoder having $N_{\text{state}}^{NC} = 2^{K'-1}$ trellis states where $K' = K - 2$ denote the effective constraint length that is a constraint length associated with selecting the PPM slot.

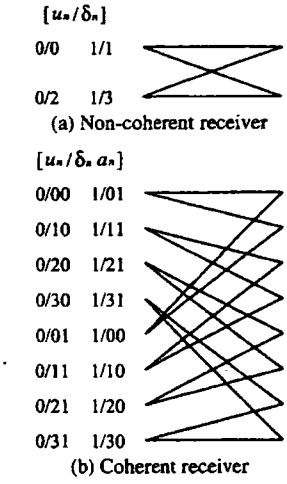

Fig. 3 Trellis diagrams ($K = 4, N_{\text{state}}^{NC} = 2, N_{\text{state}}^{C} = 8$).

Figure 3(a) shows the trellis diagram for encoder constraint length $K = 4$. The sub-optimum branch metric associated with δ_n is derived in Sect. A.2 as

$$\lambda_n(\delta_n) = y_n^{NC}(\delta_n). \tag{7}$$

In this case, the coding gain is obtained by utilizing the orthogonality between the codewords. Note that when $K = 3$ it corresponds to the uncoded transmission (i.e., $N_{\text{state}}^{NC} = 1$); therefore, no coding gain is achieved.

3.3.2 Coherent Receiver

The coherent receivers decode the received codewords by using a SOC decoder having $N_{\text{state}}^{C} = 2^{K-1}$ trellis states. Figure 3(b) shows the trellis diagram when $K = 4$. The branch metric associated with (δ_n, a_n) is computed in Sect. A.1 as

$$\lambda_n(\delta_n, a_n) = \begin{cases} y_n^C(\delta_n) & (a_n = 0), \\ -y_n^C(\delta_n) & (a_n = 1). \end{cases} \tag{8}$$

The trellis diagram in Fig. 3(b) has a property that the codewords corresponding to the two branches leaving and entering each state are antipodal, which increases the minimum distance of the code effectively. In other words, the parity bits conveyed via the polarity of the transmitted pulses increase the coding gain.

Here, it should be noted that with a given K, the number of trellis states of the non-coherent receivers is one-fourth as large as that of the coherent receivers, i.e., $N_{\text{state}}^{NC} = N_{\text{state}}^{C}/4$. This is reasonable considering that the purpose of non-coherent receivers is to reduce the complexity of the receivers.

4. Numerical Results

We evaluated the performance of the proposed scheme by means of the error rate performance in realistic UWB multipath channels. The proposed code with constraint length $K = 3, 4, 5$ is simulated. The number of PPM slots is given

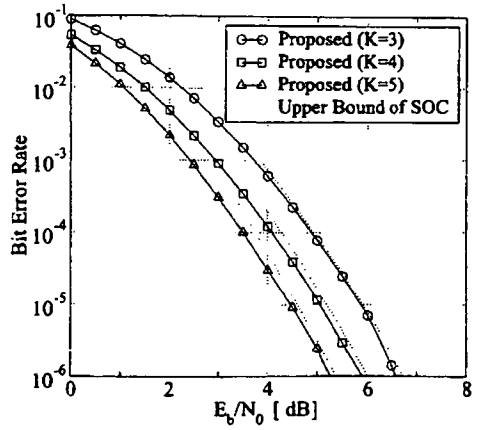

Fig. 4 Bit error rate performance of the proposed scheme (coherent receiver, AWGN channel).

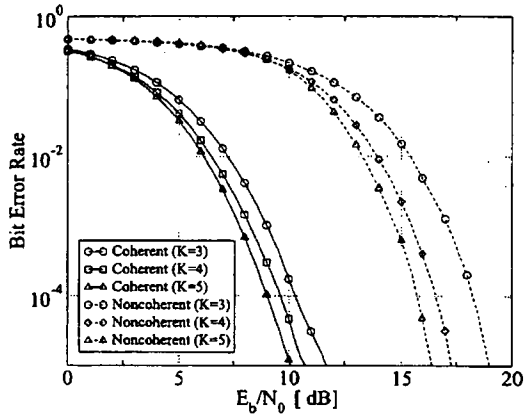

Fig. 5 Bit error rate performance for the coherent and the non-coherent receiver over multipath fading channel CM 1.

by $M = 2^{K-2}$. The error rates are averaged over 100 multipath channels in the channel model (CM) 1 [12]. For the coherent receivers, the number of RAKE fingers is $L = 8$. For the non-coherent receivers, the integration duration is $T_i = 30$ ns. We assume the bandwidth of the transmit pulses is $B = 2$ GHz. The bit duration is $T_b = 0.5\,\mu$s corresponding to the bit rate $R_b = (T_b)^{-1} = 2$ Mbps. The number of bits in a packet is $N_b = 256$ bit. The simulation results are based on soft decision Viterbi decoding.

First, Fig. 4 shows the performances of the bit error rates in terms of signal-to-noise ratio per bit, E_b/N_0, for the coherent receivers. The performance is evaluated in AWGN channel. The solid lines represent the simulation results of the proposed coherent receiver while the dotted lines represent the upper bound of SOC derived from transfer function in [4]. In this figure, the simulation results are in good agreement with the upper bounds of SOC. Therefore, this figure proves that the performance of the coherent receiver does not deteriorate due to supporting non-coherent receivers.

Figure 5 and Fig. 6 show the performances of the bit error rates and the packet error rates in terms of E_b/N_0 for both the coherent and the non-coherent receivers in multi-

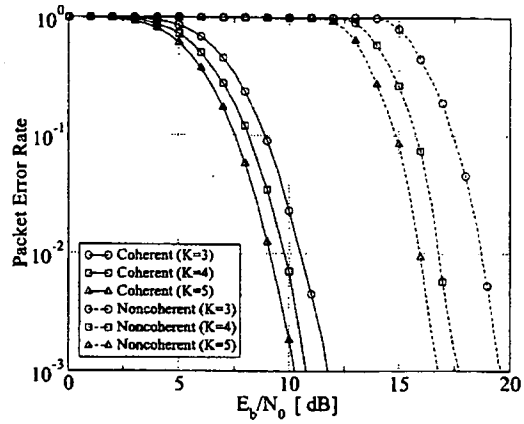

Fig. 6 Packet error rate performance for the coherent and non-coherent receiver over multipath fading channel CM 1.

path fading channel. From these results, it is observed that the error rate performance improves with the increase in the encoder constraint length for both receivers. The performance of the non-coherent receivers with $K = 3$ corresponds to the uncoded performance; thus, no coding gain is achieved. The performance of the coherent receiver is better than that of the non-coherent receiver for all value of K. One of the reason is the higher signal-to-noise ratio of the decision variables $y_n^C(m)$ compared to that of the non-coherent receivers $y_n^{NC}(m)$. The second reason is that the coherent receivers obtain a coding gain larger than that of the non-coherent receivers since the parity bits conveyed via the polarity of the transmitted pulses increase the minimum free distance of the received codewords effectively.

As mentioned before, the proposed scheme considers the systematic coding scheme in [3]† as a special case (i.e., $K = 3$); therefore, the proposed scheme can be viewed as a generalization of [3] to $K > 3$.

5. Conclusion

In this letter, we proposed a simple combined coding and modulation based on SOCs in order to support both coherent and non-coherent receivers. The error rate performances of the both coherent and non-coherent receivers were evaluated in UWB multipath channels. In the proposed scheme, the coherent receivers obtain a coding gain as large as the SOC while simultaneously supporting non-coherent receivers. In addition, their performance can be freely adapted by changing the encoder constraint length and the number of PPM slots according to its application. Thus, the proposal enables a more flexible system design for LDR-UWB systems.

Acknowledgment

This research was supported by the Japan Society for the Promotion of Science (JSPS).

†Although outer RS coding is not considered in this letter, the proposed scheme can be easily concatenated with other coding.

References

[1] G. Durisi and S. Benedetto, "Performance of coherent and non-coherent receivers for UWB communications," Proc. IEEE International Conference on Communications (ICC'04), vol.6, pp.3429–3433, June 2004.
[2] M. Schmidt, D. Simic, and R. Moorfeld, "Low complexity low data rate UWB devices -architecture and performance comparison," Proc. IST Mobile & Wireless Communications Summit, June 2005.
[3] The Institute of Electrical and Electronics Engineers, Inc. Part 15.4: Wireless Medium Access Control (MAC) and Physical Layer (PHY) Specifications for Low-Rate Wireless Personal Area Networks (LR-WPANs), Oct. 2003.
[4] A.J. Viterbi, CDMA: Principles of Spread-Spectrum Communication, Addison-Weley, Reading, MA, 1995.
[5] A.J. Viterbi, "Very low rate convolutional codes for maximum theoretical performance of spread-spectrum multiple-access channels," IEEE J. Sel. Areas Commun., vol.8, no.4, pp.641–649, May 1990.
[6] A.R. Fourouzan, M. Nasiri-Kenari, and J.A. Salehi, "Performance analysis of time-hopping spread-spectrum multipleaccess systems: Uncoded and coded schemes," IEEE Trans. Wirel. Commun., vol.1, no.4, pp.671–681, Oct. 2002.
[7] T. Matsumoto and R. Kohno, "Performance of super-orthogonal convolutional codes in multipath and multiuser channels for ultra-wideband communications," Proc. IEEE International Conference on Wireless Personal Multimedia Communications (IWS 2005/WPMC'05), Sept. 2005.
[8] T. Matsumoto, H. Ochiai, and R. Kohno, "Super-orthogonal convolutional coding with orthogonal pulse waveform for ultra-wideband communications," Proc. IEEE International Workshop on Ultra Wideband Systems Joint with Conference on Ultra Wideband Systems and Technologies (Joint UWBST&IWUWBS'04), pp.202–206, May 2004.
[9] M.L. Welborm, "System considerations for ultra-wideband wireless networks," Proc. IEEE Radio and Wireless Conf. (RAWCON'01), pp.5–8, 2001.
[10] H. Zhang and T.A. Gulliver, "Biorthogonal pulse position modulation for time-hopping multiple access UWB communications," IEEE Trans. Wirel. Commun., vol.4, pp.1536–1276, May 2005.
[11] M. Weisenhorn and W. Hirt, "Robust non-coherent receiver exploiting UWB channel properties," Proc. IEEE International Workshop on Ultra Wideband Systems Joint with Conference on Ultra Wideband Systems and Technologies (Joint UWBST&IWUWBS'04), pp.156–160, May 2004.
[12] A.F. Molish, IEEE 802.15.4a Channel Model — Final Report, IEEE TG802.15.4a, 15-04-0662-08-004a, Nov. 2004.
[13] K.G. Beauchamp, Applications of Wlash and Related Functions, Academic Press, U.S., 1984.
[14] S. Dubouloz, B. Denis, and S. Rivaz, "Performance analysis of LDR UWB non-coherent receivers in multipath environments," Proc. IEEE International Conference on Ultra-Wideband (ICU'05), pp.491–496, Sept. 2005.

Appendix: Derivation of ML Branch Metrics

A.1 Coherent Receiver

The ML branch metric for coherent receiver is derived. Let $\boldsymbol{y}^C = [y_0^C, \ldots, y_{N_b-1}^C]$. The ML decision rule is to choose the transmitted symbol corresponding to the largest of the conditional probabilities

$$p\left(\boldsymbol{y}^C|\boldsymbol{\delta}, \boldsymbol{a}\right) = \prod_{n=0}^{N_b-1} p\left(y_n^C|\delta_n, a_n\right), \tag{A·1}$$

where the right-side can be further decomposed as

$$\begin{aligned} p\left(y_n^C|\delta_n, a_n\right) &= \prod_{m=0}^{M-1} p\left(y_n^C(m)|\delta_n, a_n\right), \\ &= p_S\left(y_n^C(\delta_n)|a_n\right) \prod_{m=0, m\neq\delta_n}^{M-1} p_N\left(y_n^C(m)\right), \end{aligned} \tag{A·2}$$

where $p_S(x|a_n) = \mathcal{N}(\mu_1, \sigma^2)$ and $p_N(x) = \mathcal{N}(0, \sigma^2)$ represent Gaussian distribution where $\mu_1 = d_n A \sum_{l=0}^{L-1} |\alpha_l|^2$, and $\sigma^2 = \sum_{l=0}^{L-1} |\alpha_l|^2 N_0/2$. Taking the logarithm yields

$$\ln p\left(y_n^C|\delta_n, a_n\right) = C d_n y_n^C(\delta_n) + C'. \tag{A·3}$$

Discarding the constants C and C', the branch metric is

$$\lambda_n(\delta_n, a_n) = d_n y_n^C(\delta_n). \tag{A·4}$$

A.2 Non-coherent Receiver

Similarly to Eq. (A·2), the conditional probability of the output of the nth bit is given by

$$p\left(y_n^{NC}|\delta_n\right) = p_S\left(y_n^{NC}(\delta_n)\right) \prod_{m=0, m\neq\delta_n}^{M-1} p_N\left(y_n^{NC}(m)\right). \tag{A·5}$$

In this case, $p_S(x)$ and $p_N(x)$ have asymmetric distribution, i.e., they have non-central and central chi-square distribution with degree of freedom $2M_i$ $(= 2BT_i + 1)$ [14], respectively. The mean and variance of $p_S(x)$ and $p_N(x)$ are given by $\mu_1 = M_i N_0 + 2\mathcal{E}$, $\sigma_1^2 = M_i N_0^2 + 4\mathcal{E}N_0$ and $\mu_2 = M_i N_0$, $\sigma_2^2 = M_i N_0^2$ where $\mathcal{E}$ is the average signal energy within $0 \le t < T_i$. From the central limit theory, they are approximated as Gaussian distribution for large M_i. For simplicity, in this letter, the variances are approximated as $\sigma_1^2 = \sigma_2^2$, then the sub-optimum branch metric is given as

$$\lambda_n(\delta_n) = y_n^{NC}(\delta_n). \tag{A·6}$$

Design of the Family of Orthogonal and Spectrally Efficient UWB Waveforms

Igor Dotlić, *Member, IEEE*, and Ryuji Kohno, *Senior Member, IEEE*

***Abstract*—In this paper, a method for the design of nonlinear phase, full-band, ultra-wideband (UWB) pulses that satisfy the Federal Communications Commission's effective isotropic radiation power spectrum mask, or more generally, any other given mask, is introduced. The method uses convex programming in each step of the iterative procedure that updates the phase distribution of the goal function. Thanks to its mathematical structure, this method can be easily modified in order to be applied, in sequential fashion, to several different orthogonal UWB pulse-design problems, addressed later in the paper. The first among them is a problem considered in literature—design of multiple pulses, orthogonal when radiated. When employed for solving this problem, the method proposed here produces a considerably larger number of orthogonal pulses with high energy compared to the methods introduced before. As a novelty, the problem of designing pulses which are orthogonal in reception is considered. Then, a modification of our method is presented that can be used to solve this problem. We also introduce statistical criteria of robustness of pulses' orthogonality in reception, to the variation of the pulses' shape caused by the channel transfer function. After that, a modification of the proposed method is presented that is capable of producing a set of pulses with predefined maximum value of this criteria. Furthermore, it is shown that the method proposed can be used to efficiently design orthogonal pulses using a suboptimal value of the sample rate. All the concepts introduced are illustrated by design examples.**

***Index Terms*—FIR digital filters, orthogonal functions, optimization methods, pulse shaping, signal design, ultra-wideband (UWB).**

I. Introduction

WHEN the U.S. Federal Communications Commission (FCC) published its standard for the limitation of effective isotropic radiation power (EIRP) for ultra-wideband (UWB) systems in 2002, the problem of spectrum shaping for UWB systems came to the forefront of scientific discourse. This mask, similarly to those that are under consideration in Europe and Asia, defines power spectral density level that is very low, especially in lower frequency bands, i.e., in the global positioning system band. For this reason, in order for the UWB systems to achieve high data rates (which is imperative in applications such as wireless multimedia streaming) and/or a reasonable range, they have to utilize the defined spectrum mask efficiently. More precisely, they have to use a given frequency-time channel[1] capacity efficiently. In pulse-modulated UWB systems, this means that the radiated pulse has to be spectrally efficient, i.e., it has to have as much energy as possible while being compliant with a given spectrum mask.

A technique that can be used additionally for improving UWB pulse system capacity is to use multiple pulse waveforms that are mutually orthogonal. This can be done either in a M-ary signaling system where one member of a signaling set (set of M orthogonal UWB pulses) is radiated at the time, or by using a signaling scheme in which each pulse from the set is used as a carrier for some pulse amplitude modulation (PAM), usually binary phase shift keying (BPSK), and pulses are radiated simultaneously. Moreover, in a multiuser environment, as shown in [1], a higher capacity can be achieved if each user utilizes a signaling set that consists of pulses that are orthogonal to those used by other users in the system.

All these opened the problem of the design of a set of UWB pulses that are mutually orthogonal and optimally exploit the available spectrum mask. A set of the orthogonal UWB pulse waveforms, based on the modified Hermite polynomials (HP) is introduced in [1]. However, as shown in [2], in order for the modified HP pulses to comply with the FCC's spectrum mask, both filtering and up-conversion has to be done. An attempt to solve the problem described in the discrete-time domain has been presented in [3], using pulses that are eigenvectors corresponding to the largest eigenvalues of a matrix calculated by sampling FCC's spectrum mask. However, the number of pulses generated was only two and the FCC's spectrum mask was not exploited optimally. By using the discrete-time prefiltering paradigm, different methods, originally developed for the design of the FIR digital filters in frequency domain, were applied for the design of the spectrally efficient UWB waveforms [4]–[7]. In [4], the FCC mask compliant UWB waveforms were designed by applying the Parks-McClellan algorithm, referred to as a "workhorse of digital filter design methods". In [6] and [7], FCC mask compliant waveforms, optimal in the sense of spectral efficiency for a given pulse duration, were designed by using the semi-definite programing (SDP). In [5] and [7], families of the orthogonal UWB waveforms that comply with the FCC's spectrum mask, were designed by using second-order cone programing (SOCP). However, since the method described in [5] and [7] is limited to the waveforms with linear phase, the number of waveforms designed was relatively small. Furthermore, the spectral efficiency decreased rapidly with the increase of the index of a designed orthogonal pulse waveform.

This motivated us to search for a UWB pulse-waveform design method that can produce a family of orthogonal, full-band

Manuscript received August 31, 2006; revised January 26, 2007. This work was supported by the by the Japan Society for the Promotion of Science (JSPS). The associate editor coordinating the review of this manuscript and approving it for publication was Dr. Arye Nehorai.

The authors are with the Division of Electrical and Computer Engineering, Yokohama National University, 240-8501 Yokohama, Japan (e-mail: dotlic@ieee.org; kohno@ynu.ac.jp).

Digital Object Identifier 10.1109/JSTSP.2007.897045

[1]We consider here only systems with single antenna per user and therefore only frequency-time channels.

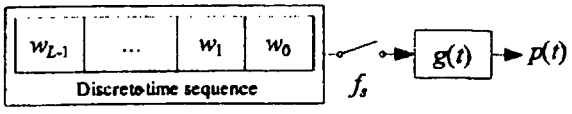

Fig. 1. Pulse-design model under consideration.

UWB pulses that, on one hand, have members with relatively high spectral efficiency, and on the other, are as many as possible. The method that will be described here, similarly to [4]–[7], uses the discrete-time prefiltering paradigm for the UWB pulse shaping. Also, similarly to [5] and [7], it is based on the SOCP. However, unlike [5] and [7], our method is not limited to designing pulses with a linear phase distribution. Furthermore, in contrast with [5] and [7], our method uses a full vector of filter coefficients as the optimization variable. For these reasons, in the sequential design procedure, crosscorrelation between pulse being designed and arbitrary waveform(s) can be constrained in the time domain. For a given set of time shift(s), crosscorrelation between a pulse that is being designed and some other, previously designed pulse(s), can be constrained to be equal to zero. Furthermore, maximum and mean-square levels of pulses crosscorrelation for a predefined time-shift interval can be upper bounded. Our method also enables for orthogonality among pulses to be imposed, not only when they are radiated, as in [3], [5], and [7], but also in detection. This also, unlike before, gives one the ability to construct a set of UWB pulses, the orthogonality of which is robust to variations of multipath channel characteristics along different paths.

The rest of the paper is organized as follows. In Section II, a description of the system model, used in the paper, is presented. Then, in Section III, we derive orthogonal pulse-design methods for different criteria that correspond to different communications scenarios. Section IV provides examples of the pulse designed with methods presented in previous sections. At the end, conclusions are deduced from our presented results.

II. System Model

A. Pulses When Radiated

In this work, we use a UWB pulse-design model shown on Fig. 1, similar to that used in [4]–[7].[2] Let us denote the real discrete-time sequence of length L as a column vector: $\mathbf{w} = [w_l]_{l=0}^{L-1} \in \Re^L$. This discrete-time sequence is interfaced, with a sample rate $f_s = 1/T_s$, to the analog system with pulse response equal to $g(t)$. The designed UWB pulse waveform, when radiated, represents pulse response of the overall system

$$p(t) = \sum_{l=0}^{L-1} w_l g(t - lT_s). \tag{1}$$

This can be rewritten in the vector form as

$$p(t) = \mathbf{g}(t)^T \mathbf{w}, \tag{2}$$

[2]Different implementation aspect of this concept were discussed in [4].

where $\mathbf{g}(t) = [g(t), g(t-T_s), \ldots, g(t-(L-1)T_s)]^T$. Duration of the pulse can be expressed as

$$T_p = T_g + (L-1) \times T_s \tag{3}$$

where T_g is the duration of $g(t)$.

In impulse-based UWB systems, it is customary to use signaling with a periodic time-hopping (TH) spreading sequence in order to minimize the effects of multi-access interference (MAI) and distribute it evenly among all users in the system. Effects of the TH spreading sequence on the EIRP spectrum of the pulse-based UWB systems have been analyzed in [2] and [4]. In [4], it has been shown that, for systems with the periodic TH spreading sequence and either BPSK or PPM, the EIRP spectrum can be approximated by the scaled version of the power spectrum of the pulse being radiated

$$\Phi_{\mathrm{EIRP}}(f) \approx \frac{\mathcal{E}_s}{T_f} |P(f)|^2. \tag{4}$$

$\Phi_{\mathrm{EIRP}}(f)$ is the EIRP spectrum of the UWB system, $P(f)$ is the spectrum of the pulse being radiated in the system, and $\mathcal{E}_s$ and T_f are constants representing symbol energy and frame period respectively. According to (2), $P(f)$ can be expressed in the following form:

$$P(f) = W(f)G(f). \tag{5}$$

Here, $G(f)$ is Fourier transform of $g(t)$, $W(f)$ can be expressed in the vector form as

$$W(f) = \mathbf{v}(f)^H \mathbf{w}. \tag{6}$$

$\mathbf{v}(f)$ is the Fourier kernel column vector that can be written as $\mathbf{v}(f) = [\exp(j2\pi fl/f_s)]_{l=0}^{L-1}$. Consider now two pulses, shaped in the described way, denoted by n and k, respectively: $p_n(t) = \mathbf{g}(t)^T \mathbf{w}_n$ and $p_k(t) = \mathbf{g}(t)^T \mathbf{w}_k$. Crosscorrelation between them, when they are radiated, $C_{k,n}^g(\tau)$, is defined as

$$C_{k,n}^g(\tau) := \int_{-\infty}^{+\infty} p_k(t) p_n(t+\tau)\, dt. \tag{7}$$

If the autocorrelation function of $g(t)$ is denoted $R_g(t)$, substituting (2) in (7) results in

$$C_{k,n}^g(\tau) = \mathbf{w}_k^T \mathbf{R}_g(\tau) \mathbf{w}_n. \tag{8}$$

Here, $\mathbf{R}_g(\tau)$ is the $L \times L$ Toeplitz matrix of $R_g(\tau)$: $\mathbf{R}_g(\tau) = [R_g(\tau + (i-j)T_s)_{i,j}]_{L \times L}$.

B. Pulses in Reception

Indoor UWB channel is usually modeled as a real multipath channel

$$a(t) = \sum_{m=1}^{\infty} a_m \delta(t - T_m). \tag{9}$$

Here $a_m \in \Re$ is the amplitude of mth multipath component and $T_m \in \Re^+$ is its delay time. Standard IEEE P802.15.3a

indoor channel model [8] describes time and amplitude distribution of multipath components. Regarding pulses' orthogonality, pulse-shape distortion due to factors like non-omnidirectional antenna characteristics, reflections from and propagation through different materials can be interesting. However, these pulse-shape distortion types are not included in the IEEE P802.15.3a channel model. For this reason, we chose to modify the standard model (9) and replace $\delta(t - T_m)$ with the factor $u_m(t - T_m)$. This factor does not only describe delay, but also pulse-shape distortion of the mth multipath component

$$a(t) = \sum_{m=1}^{\infty} a_m u_m(t - T_m). \tag{10}$$

Since there is no statistical model known to the authors that covers the described phenomena, a simple model is used. In the model, $u_m(t)$ is assumed to be zero-mean and a nearly white random process, with the time-dependent power

$$E\{u_m(t)\} = 0 \tag{11a}$$
$$E\{u_m(t)^2\} = \sigma_u(t)^2 \tag{11b}$$
$$E\{u_m(t)u_m(t+\tau)\} \approx 0 \tag{11c}$$

for $m = 1, \ldots, \infty, \tau \neq 0, t \in [-\infty, +\infty]$. Let us denote the receiver's pulse response as $h(t)$ and $b(t) = g(t) \otimes h(t)$. Total response of the continuous-time portion of the system can be expressed as

$$c(t) = b(t) \otimes a(t). \tag{12}$$

If the pulse shaper shown in Fig. 1 is used in a transmitter, according to (10) and (12), the received pulse will have a form

$$r(t) = \mathbf{b}(t)^T \mathbf{w} \otimes \sum_{m=1}^{\infty} a_m u_m(t - T_m). \tag{13}$$

Here, $\mathbf{b}(t) = [b(t), b(t - T_s), \ldots, b(t - (L-1)T_s)]^T$.

Consider now a UWB system in which multiple pulses, of the form (2) and (13), denoted by the index, are used. Pulses can be radiated simultaneously, e.g., as quasi-orthogonal BPSK carriers, or one at the time[3] . For both signaling schemes, we will assume that a RAKE receiver with an arbitrary number of fingers is used. A template waveform of the RAKE receiver is made according to a known part of the pulse with the index k

$$q_k(t) = \mathbf{b}(t)^T \mathbf{w}_k. \tag{14}$$

An assumption is made that fingers of the RAKE receiver are synchronized with multipath components that are at least T_p spaced from other multipath components. If the pulse with index n is transmitted, the output of the correlator that corresponds to the mth multipath component will be

$$D_{k,n}^m(\tau) = a_m \mathbf{w}_k^T \mathbf{R}_b(\tau) \mathbf{w}_n \otimes u_m(\tau). \tag{15}$$

[3]This signaling scheme was proposed in [1] and is denoted as the orthogonal pulse modulation (OPM).

$\tau = 0$ is the moment of decision, while $\mathbf{R}_b(\tau)$ represents the Toeplitz matrix of autocorrelation of $b(t) - R_b(\tau)$, $\mathbf{R}_b(\tau) = [R_b(\tau + (i-j)T_s)_{i,j}]_{L \times L}$. Similarly to (7), $C_{k,n}^b(\tau)$ can be defined as

$$C_{k,n}^b(\tau) := \mathbf{w}_k^T \mathbf{R}_b(\tau) \mathbf{w}_n. \tag{16}$$

Hence, (15) can be rewritten as

$$D_{k,n}^m(\tau) = a_m C_{k,n}^b(\tau) \otimes u_m(\tau). \tag{17}$$

From (11) and (17), the first- and second-order output statistics of the $D_{k,n}^m(\tau)$, in the moment of decision, can be derived as

$$E\left\{D_{k,n}^m(0)\right\} = 0 \tag{18a}$$
$$E\left\{D_{k,n}^m(0)^2\right\} = E\left\{a_m^2\right\} \int_{-\infty}^{+\infty} C_{k,n}^b(\tau)^2 \sigma_u(\tau)^2 \, d\tau. \tag{18b}$$

From (18b), it is clear that the ratio of $E\{D_{k,n}^m(0)^2\}$ for different values of k and n does not depend on m. Therefore, without loss of generality, we may assume $E\{a_m^2\} = 1$ and rewrite (18b) as

$$E\{D_{k,n}(0)^2\} = \int_{-\infty}^{+\infty} C_{k,n}^b(\tau)^2 \sigma_u(\tau)^2 \, d\tau. \tag{19}$$

It will be useful in the following text to rewrite (19) as a quadratic form with respect to $\mathbf{w}_n$:

$$E\{D_{k,n}(0)^2\} = \mathbf{w}_n^T \mathbf{A}_k \mathbf{w}_n \tag{20}$$

where $\mathbf{A}_k = \int_{-\infty}^{+\infty} \mathbf{R}_b(\tau) \mathbf{w}_k \mathbf{w}_k^T \mathbf{R}_b(\tau) \sigma_u(\tau)^2 \, d\tau$. Since $\mathbf{A}_k$ is a positive semi-definite matrix, by using eigen decomposition [9], matrix $\mathbf{B}_k$ can be found which satisfies: $\mathbf{A}_k = \mathbf{B}_k^T \mathbf{B}_k$. Hence, (20) can be written as

$$E\{D_{k,n}(0)^2\} = \|\mathbf{B}_k \mathbf{w}_n\|^2 \tag{21}$$

which is the square of the second-order cone (SOC) with respect to $\mathbf{w}_n$.

III. Optimization Techniques

A. Single-Pulse Design

In [6] and [7], nonlinear phase pulses that satisfy FCC's spectrum mask, optimal in the sense of spectral efficiency, were designed using SDP. Nevertheless, the method described in [6] and [7] uses the autocorrelation vector of $\mathbf{w}$ as the optimization variable. For this reason, by using a convex optimization toolbox, like [10], it is not possible to impose orthogonality with any other waveform as the optimization constraint. On the other hand, in [5] and [7], optimization was done in the domain of $\mathbf{w}$ itself. However, the convex optimization formulation used was limited to pulses with linear phase distribution and used only half elements of $\mathbf{w}$ as the optimization variable. For these reasons, spectral efficiency of higher order pulses decreased rapidly as their index grew. In this work, our idea was to find a convex optimization based method that can produce nonlinear phase

waveforms using the full w vector as the optimization variable. Then, it will be easy to impose the orthogonality requirement with other pulses as equality constrains in sequential design procedure. For a single pulse, the goal of the optimization is to maximize the spectral utilization factor ψ of available power under the given EIRP mask's $S(f)$ main lobe[4] F_p, as defined in [5]–[7]

$$|P(f)| \leq \sqrt{S(f)} \quad \forall f, \tag{22a}$$

$$\max_{\mathbf{w}} \psi = \frac{\int_{F_p} |P(f)|^2 df}{\int_{F_p} S(f) df}. \tag{22b}$$

Similarly to [5] and [7], (22a) is not satisfied and (22b) is not optimized in the continuous domain, but rather in the large enough number of discrete optimization points $N = 15L$. Optimization points are uniformly distributed between 0 and $f_s/2$. As in [5] and [7], $S(f)$ is replaced with its more strict version $S_a(f)$ so that possible spectral regrowth due to the system's nonlinearity is taken into account. Since this phenomenon affects areas of the shaped power spectrum with low power levels (outside the main lobe), there the used spectrum mask is more strict than original.[5] Furthermore, maximization of ψ is not done directly, but rather by the minimization of the difference between $S(f)$ and $|P(f)|^2$ in the F_p

$$\min_{\mathbf{w}} \gamma = \sqrt{\sum_{f_k \in F_p} S_a(f_k) - |P(f_k)|^2} \tag{23a}$$

$$|P(f_k)| \leq \sqrt{S_a(f_k)}, \quad f_k = \frac{kf_s}{2N}, \quad 0 \leq k \leq N-1. \tag{23b}$$

Each constraint in (23b) can be represented as a single quadratic constraint in the convex optimization toolbox [10]. However, the problem defined with (23) is non-convex and therefore cannot be rewritten in the form suitable for implementation in the convex program. Nevertheless, the convex problem, similar to (23), can be defined

$$\min_{\mathbf{w}} \gamma = \sqrt{\sum_{f_k \in F_p} \left| e^{j\phi_S(f_k)} \sqrt{S_a(f_k)} - P(f_k) \right|^2} \tag{24}$$

subject to (23b).

Here, a predefined phase factor $e^{j\phi_S(f)}$ is assigned to the $\sqrt{S_a(f)}$ and the power of difference between $e^{j\phi_S(f)}\sqrt{S_a(f)}$ and $P(f)$ is minimized. In the convex optimization toolbox [10], the sum in (24) can be implemented as a single rotated second order cone constraint. Optionally, the problem can be transformed so that the dimension of this rotated second order cone constraint is lowered [5], [7].

In [5] and [7], a strategy was proposed to set linear phase distributions prior to the optimization via Hadamard orthogonal binary codes in order to have corresponding pulses obtained from the optimization that are "essentially orthogonal". However, as discussed in [5] and [7], each crossing of Hadamard code between its binary states produces null in the power spectrum of the corresponding pulse. For this reason, spectral efficiency of designed pulses decreased rapidly as their index grew. Here, we will adopt a different approach, and iteratively change nonlinear phase distribution in order to get the maximum ψ possible. The proposed optimization procedure can be described in the following steps.

1) Set $\gamma' = 0$ and initial phase distribution to zero: $\phi_S(f_k) = 0, \forall f_k \in F_p$.[6]
2) Solve optimization problem (24), obtaining w and γ.
3) Test convergence criteria: If $|\gamma' - \gamma|/\gamma \leq \delta$, go to 7).
4) Update phase distribution: $\phi_S(f_k) = \angle(P(f_k)) = \angle(\mathbf{v}(f_k)^H \mathbf{w} G(f_k)), \forall f_k \in F_p$.
5) $\gamma' = \gamma$.
6) Go to 2).
7) End.

Therefore, the primary differences of our method from the one described in [5] and [7] are as follows.

1) The full vector of the filter coefficients (w) is used as the optimization variable, in contrast with [5] and [7], where only half elements of this vector are used.
2) The pulse's phase distribution is nonlinear and iteratively exchanged during the optimization process, in contrast with [5] and [7], where it is linear and predefined.

All advantages of our pulses, that will be described in the following text, come from these features. The procedure described above is not proved to be optimal in the sense of maximizing ψ. Nevertheless, as design examples will show, ψ achieved with the method proposed is always higher than one achieved with method from [5] and [7]. Typically, for $\delta = 0.1\%$, the method proposed converges in up to 15 iterations, as shown in Fig. 2.

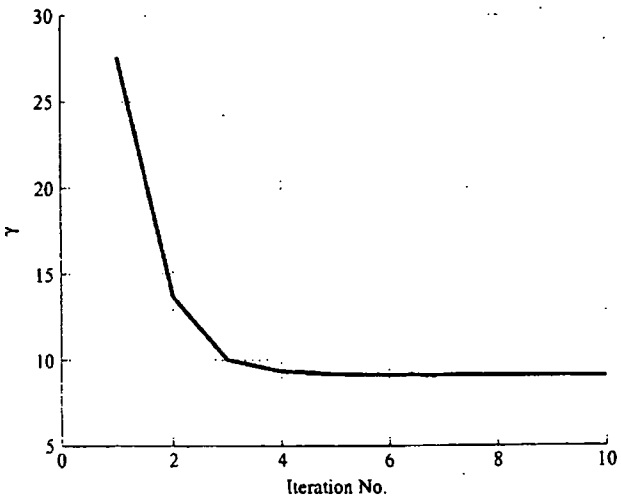

Fig. 2. Typical convergence curve of the proposed method.

[4]For FCC mask $F_p = \{f_p \mid f_p \in [3.1, 10.6]\ \text{GHz}\}$

[5]In the main lobe, $S_a(f)$ is the same as $S(f)$. In the area of side lobes, $S_a(f)$ is set to be at least 5 dB below $S(f)$ in order for the spectral regrowth due to the system nonlinearities to be taken into account.

[6]During research, it has been found that setting the initial phase distribution to linear: $\phi_S(f_k) = -\pi(L-1)f_k/f_s, \forall f_k \in F_p$, results in the algorithm staying fixed to the linear-phase solution, which is suboptimal in the sense of maximizing ψ. Although, naturally, convergence is achieved in a single iteration.

B. Multiple Orthogonal Pulses Design

As in [3], [5], and [7], orthogonality among radiated pulses is defined as zero crosscorrelation for zero time shift. In contrast with [5] and [7], the procedure described above uses the full vector of filter coefficients $\mathbf{w}$ as the optimization variable. For this reason, it is easy to add equality constraints to the convex optimization in step 2) that will ensure orthogonality of the pulse being designed with an arbitrary set of waveforms. Therefore, pulses may be designed sequentially, while the orthogonality of pulse being designed at the current sequence step with the set of pulses designed previously is ensured by adding appropriate equality constraints to the optimization problem.

Let us denote designed vectors $\mathbf{w}$ by their index in the design sequence: $\mathbf{w}_1, \mathbf{w}_2, \mathbf{w}_3, \ldots$. In the first step-optimization of $\mathbf{w}_1$, the pulse of predefined parameters: $f_s, L, S_a(f)$ and $G(f)$ is designed using the procedure from the previous subsection. In other words, no constraints that impose orthogonality with other pulses are added to the optimization problem. In every following step, convex optimization problem (24) is modified by adding equality constraints that ensure orthogonality with the pulses that have an index lower than the pulse being designed. For the nth pulse, according to (8), this can be written as

$$C^g_{k,n}(0) = \mathbf{w}_k^T \mathbf{R}_g(0)\mathbf{w}_n = 0, \quad \text{for } k = 1, \ldots, (n-1). \tag{25}$$

Alternatively, by using the method proposed here, orthogonality between pulses in detection can be also attained. Naturally, a strict orthogonality in detection may be sought only if the transfer function of each channel path can be approximated to be the same and completely known, i.e., $u_m(t) = \delta(t)$, for $m = 1, \ldots, \infty$. Then, according to (15), instead of (25), the equality constrains that impose orthogonality in detection can be added to the described sequential design procedure

$$C^b_{k,n}(0) = \mathbf{w}_k^T \mathbf{R}_b(0)\mathbf{w}_n = 0, \quad \text{for } k = 1, \ldots, (n-1) \tag{26}$$

while the rest of the procedure remains the same.

C. Channel Robust Orthogonal Pulse Design

By using the model introduced in Section II-B, it is possible to design a set of waveforms, the orthogonality of which is robust to channel variations. In other words, it is possible to design a set of pulses that will have the output of the RAKE receiver for each pulse robust to interference produced by synchroneously receiving other pulses instead of the desired one. Again, the design procedure is sequential, with each step in the sequence corresponding to the design of a single pulse, i.e., its vector $\mathbf{w}_n$. However, what is different, is that now, constraints being added to step 2) of the numerical procedure introduced in Subsection III-A are not an equality but SOC. According to (21), the SOC constraint which bounds $E\{D_{k,n}(0)^2\}$ can be added to the convex program that optimizes $\mathbf{w}_n$

$$\|\mathbf{B}_k \mathbf{w}_n\| \leq \alpha \|\mathbf{B}_k \mathbf{w}_k\|, \quad \text{for } k = 1, \ldots, (n-1) \tag{27}$$

which is equivalent to

$$E\{D_{k,n}(0)^2\} \leq \alpha^2 E\{D_{k,k}(0)^2\}, \quad \text{for } k = 1, \ldots, (n-1). \tag{28}$$

Therefore, a mean power of interference introduced to the output of the RAKE receivers matched to previously designed members of the sequence is bounded to be less or equal to α^2 portion of the power when the receivers' corresponding pulses are received. The choice of α can be between values in the range $0 < \alpha < 1$. As the design examples show, it is a compromise between a loss in spectral efficiency of waveforms with higher indeces and interference introduced in the system (28).

D. Orthogonal Pulses Design With Suboptimal Sample Rate

By using the method proposed here, similarly to [4], pulses can be designed using a smaller sample rate than necessary according to the general signal processing theory. This is possible because, on the one hand, the desired spectrum shape in the pass-band is flat, and on the other, the spectrum of $g(t)$ is approximately symmetrical in F_p. Furthermore, by choosing $f_s = 2 \times f_g$, $|W(f)|$ can also be made to be symmetrical with respect to f_g. This results in having an overall spectrum of $P(f)$ that is approximately symmetrical in F_p. Since now $|W(f_g + f)| = |W(f_g - f)|$, the pulse spectrum is bounded by stricter of these constraints

$$|P(f_g + f)| \leq \sqrt{S_a(f_g + f)} \tag{29a}$$

$$|P(f_g - f)| \leq \sqrt{S_a(f_g - f)}, \quad \forall |f| \leq f_g. \tag{29b}$$

This makes the designed pulse suboptimal in the sense of maximizing ψ for a given pulse duration. Outside of F_p, this results in having spectrum sidelobes the level of which is practically bounded by the lower frequency part of $\sqrt{S_a(f)}$.

On top of being able to design single pulse with suboptimal f_s, the method proposed here can be used to design a set of multiple orthogonal pulses with suboptimal f_s. A modification of the original single pulse-design technique is the same as that described in Sections III-B and III-C.

Theoretically, the method from [5] and [7] could be also used with a suboptimal sample rate. However, with $f_s = 2 \times f_g$, the number of nulls in the spectra of the designed pulses with an order higher than one would double. This would make the pulses' spectral efficiency decrease even faster than in the case when high f_s is used.

IV. Design Examples

A. Multiple Orthogonal Pulses Design Examples

For the design examples, we used a system with the same parameters as one used in [5] and [7]: $g(t)$ is set to be first order Gaussian monocycle with frequency corresponding to the maximum of $G(f)$ equal to $f_g = 6.85$ GHz, which is the center frequency of the FCC's mask passband. The sampling frequency of the discrete-time filter is set to be $f_s = 28$ GHz.

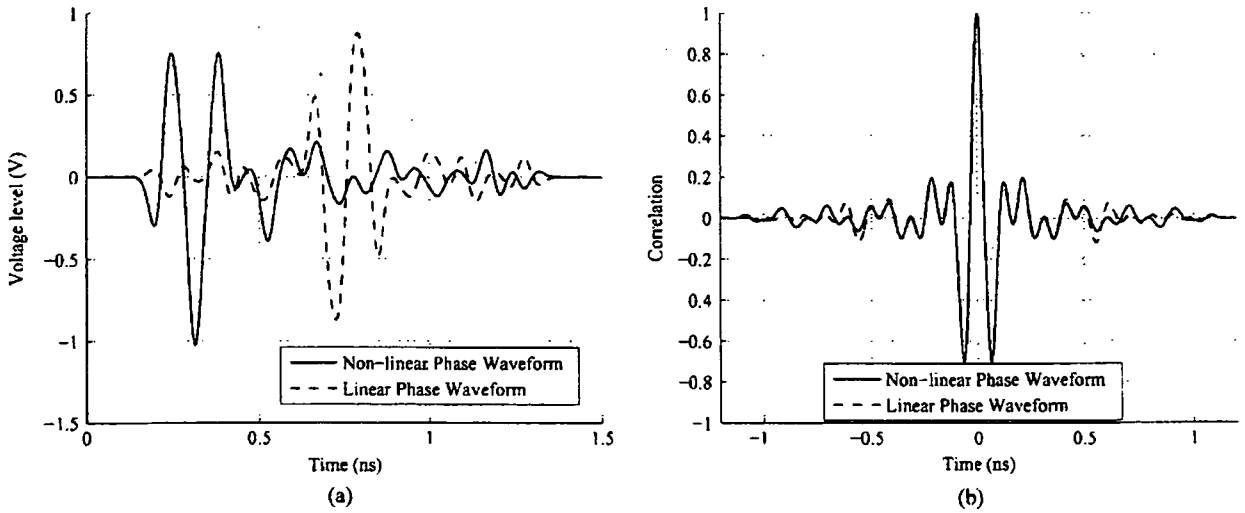

Fig. 3. Time-domain properties of designed linear and nonlinear phase pulses. (a) Pulse waveforms. (b) Autocorrelation properties.

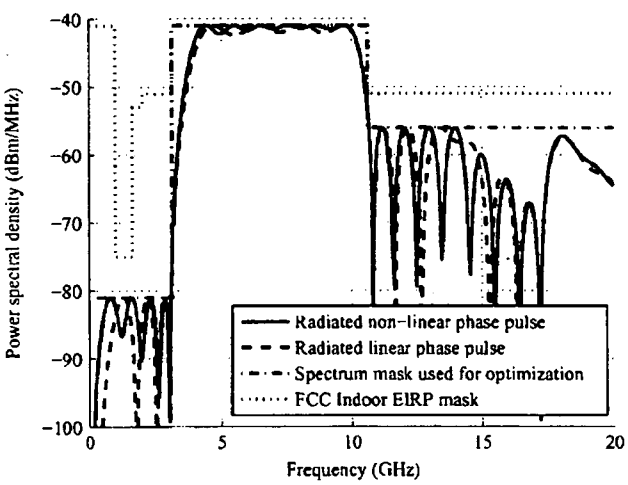

Fig. 4. Spectra of the designed nonlinear and linear phase pulses.

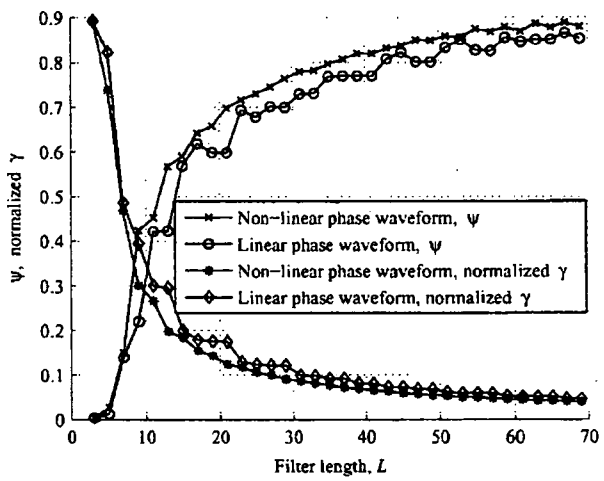

Fig. 5. ψ and γ attained with linear and nonlinear phase waveform design.

Fig. 3 shows time domain characteristics of the first order designed linear and nonlinear phase pulses for $L = 31$. Both pulses exhibit similar properties in waveform shape and autocorrelation. Furthermore, as Fig. 4 shows, the spectra of both waveforms look similar. The nonlinear phase waveform attains somewhat higher ψ regardless of the designed pulse duration, i.e., L used in the design process, which can be observed in Fig. 5.

Another thing that can be seen in Fig. 5 is that the problem of constrained maximization of ψ (22) is not completely equivalent with the problem of constrained minimization of γ (24). Although γ attained with both linear and non--linear phase waveforms design uniformly decreases with the increase of L, this is not a case with an increase of ψ. Waveforms of designed lower order orthogonal linear and nonlinear phase pulses can be seen on Fig. 6.

A similarity between orthogonal pulses designed with the method proposed here and the one from [5] and [7] decreases as the index of the pulse increases. That is, the energy of designed linear-phase pulses from [5] and [7], i.e., their ψ, decreased very rapidly with the increase of the waveform index. On the other hand, nonlinear phase waveforms with lower indices sustain relatively high ψ. This is due to nulls introduced in the spectra of linear-phase waveforms in F_p (Fig. 8). For the same reason, autocorrelation properties of linear phase pulses from [5], [7] look somewhat better (Fig. 7). That is, because of the finite energy property of pulses with the high ψ (see Appendix A), nonlinear phase waveforms have energy of crosscorrelation between them approximately equal to the energy of their autocorrelations. On the other hand, nulls that appear at different points of the spectra of linear phase pulses from [5] and [7] make the energy of their crosscorrelation somewhat lower.

The ability of the method proposed here to produce a relatively large set of orthogonal pulses that preserve high ψ can be observed in Figs. 9 and 10; there, time and spectral domain characteristics of the higher order pulses are shown. Pulses preserve high ψ and similar spectral and time-domain characteristics to lower-order pulses up to the pulse with index ten. This does not hold for orthogonal linear-phase pulses designed with the method from [5] and [7]. The exact ψ achieved depending on

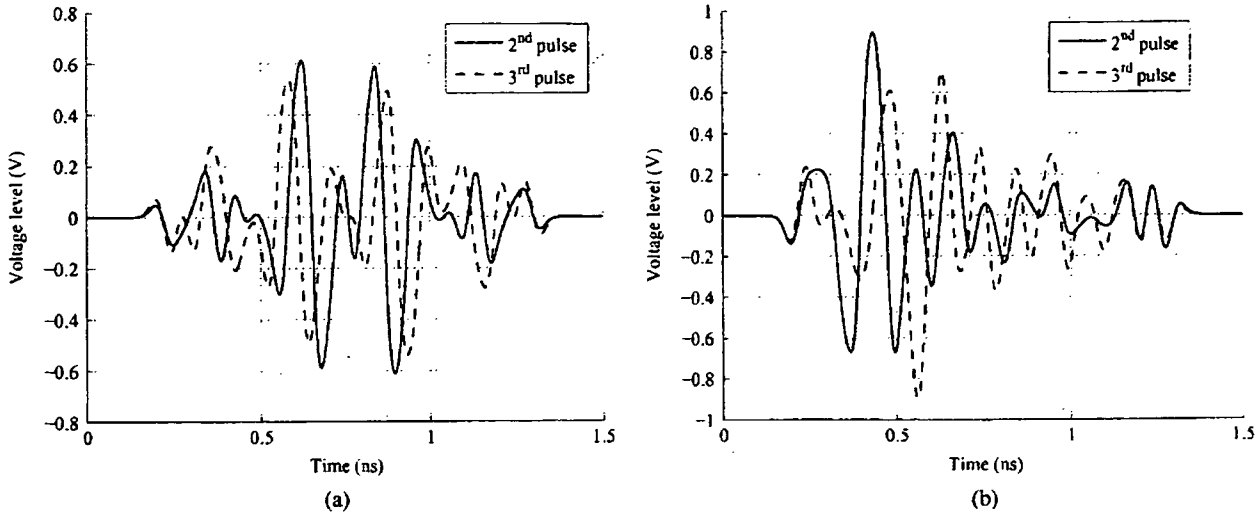

Fig. 6. Waveforms of designed lower order orthogonal linear and nonlinear phase pulses. (a) Linear phase pulses. (b) Nonlinear phase pulses.

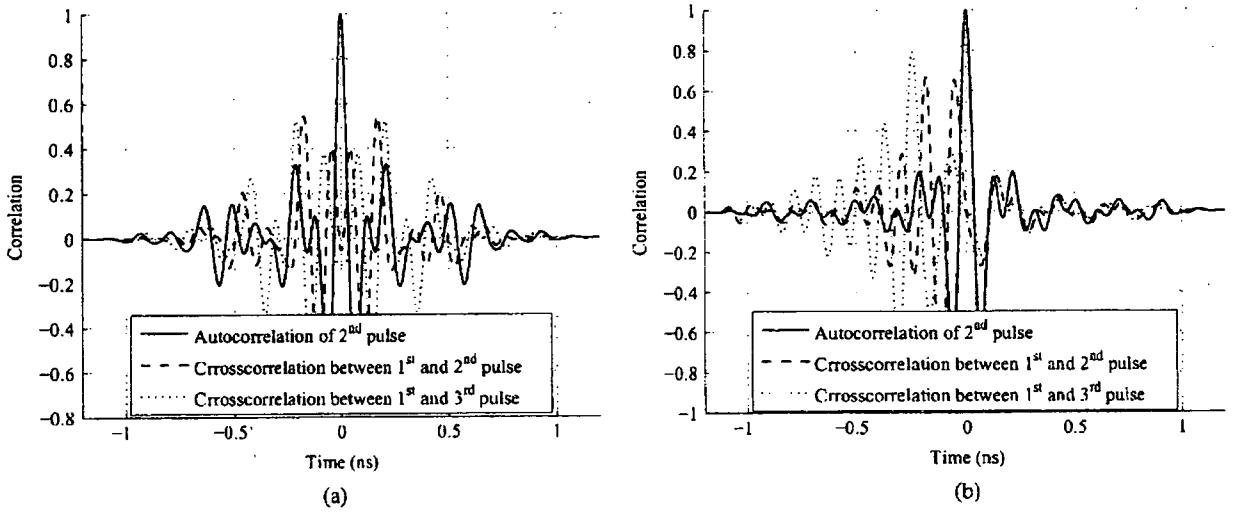

Fig. 7. Correlation properties of designed lower order orthogonal linear and nonlinear phase pulses. (a) Linear phase pulses. (b) Nonlinear phase pulses.

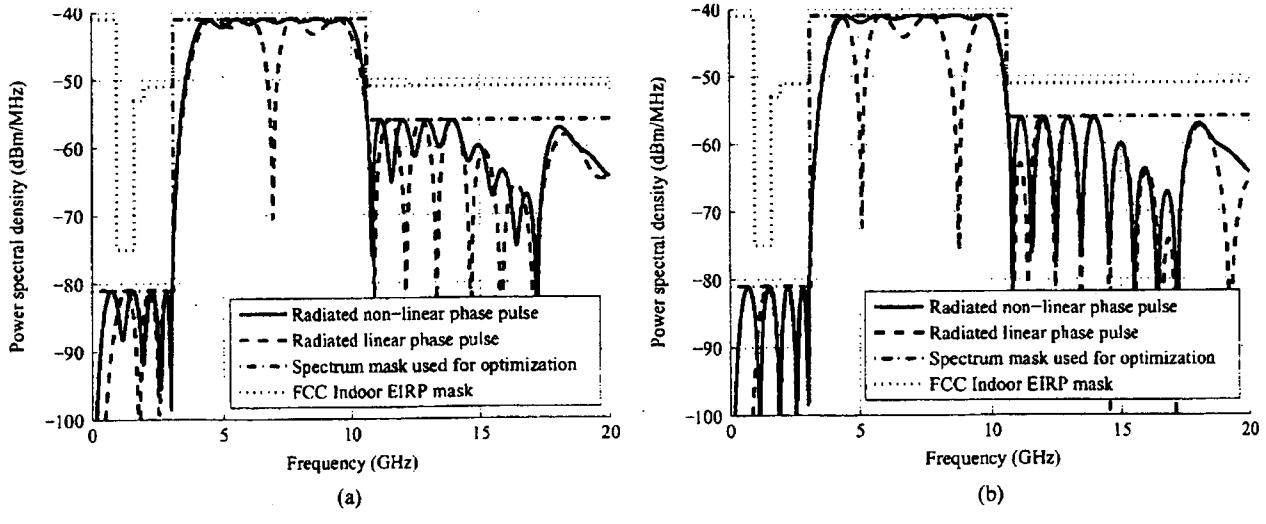

Fig. 8. Spectra of designed lower order orthogonal linear and nonlinear phase pulses. (a) Second pulses. (b) Third pulses.

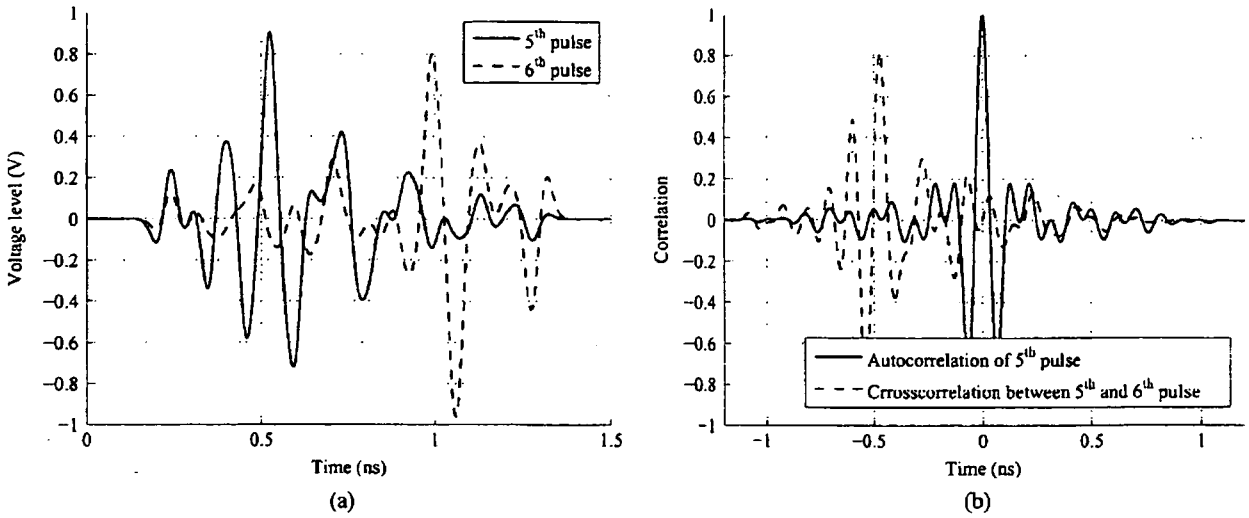

Fig. 9. Time-domain properties of designed higher order orthogonal nonlinear phase pulses. (a) Pulse waveforms. (b) Correlation properties.

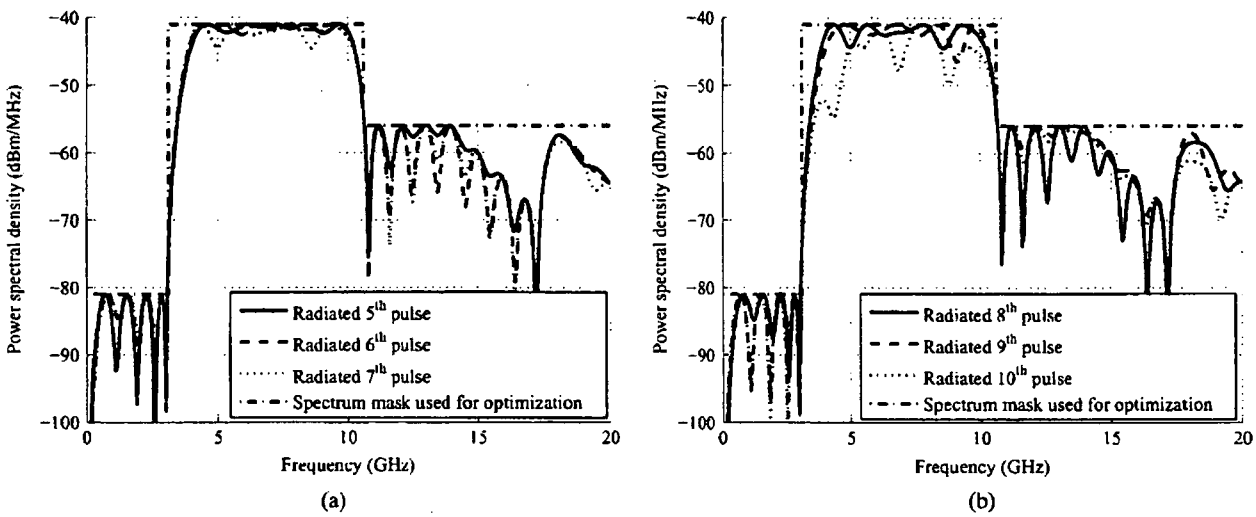

Fig. 10. Spectra of designed orthogonal higher order nonlinear phase pulses. (a) Fifth, sixth, and seventh pulse. (b) Eight, ninth, and tenth pulse.

the waveform index, for different values of L and two methods considered, is shown in Fig. 11. Since ψ for the method from [5] and [7] decreases very quickly with the increase of the waveform index, only the first three designed waveforms are shown.

B. Robust Orthogonal Pulses Design Examples

For the design of pulses that have orthogonality that is robust to pulse-shape distortions, we used the same system as in Section IV-A with $L = 31$. As $b(t)$, we used the Gaussian pulse which is integral of the Gaussian Monocycle, used before as $g(t)$. This is founded upon a well-known first approximation of UWB antenna—as a differentiator in transmission and integrator in reception. $\sigma_u(t)$ is also modeled as a Gaussian curve: $\sigma_u(t) = \exp(-2t^2/\tau_u^2)$, where $\tau_u = 100$ ps.

In Fig. 12(a), it can be observed that the energy of the pulses' crosscorrelation function is moved from the area that has a value of $\sigma_u(t)$ that is significantly larger than zero. For a larger α, this is even more pronounced. However, as Fig. 12(b) shows, with

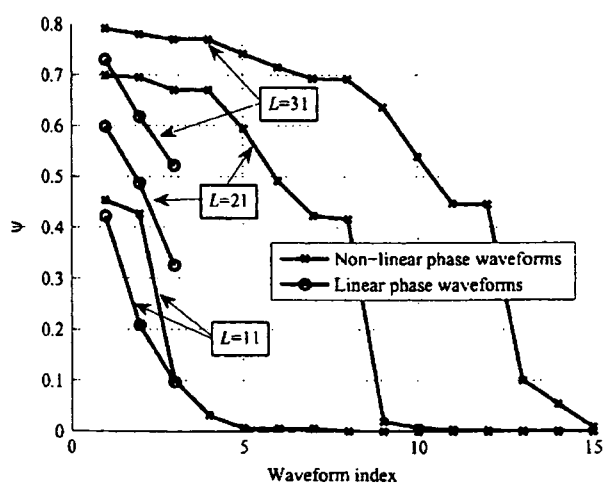

Fig. 11. Achieved ψ by designed orthogonal nonlinear and linear phase waveforms for different L.